UNIVERSITY OF CALIFORNIA SAN DIEGO

Physical Reservoir Computing in Photonics Integrated Circuit

A Dissertation submitted in partial satisfaction of the requirements
for the degree Doctor of Philosophy

in

Electrical Engineering (Photonics)

by

Chengkuan Gao

Committee in charge:

Professor Yeshaiahu Fainman, Chair
Professor Tzu-chien Hsueh
Professor Zhaowei Liu
Professor Yu-hwa Lo
Professor David Saintillan

2024

The Dissertation of Chengkuan Gao is approved, and it is acceptable in quality and form for publication on microfilm and electronically.

University of California San Diego

2024

DEDICATION

IN MEMORY OF THE LOVE OF MY LIFE

司文 SI WEN

1995 05 25 — 2023 05 10

TABLE OF CONTENTS

LIST OF FIGURES

LIST OF TABLES

ACKNOWLEDGEMENTS

I would like to acknowledge all my family, friends, and everyone in my group, I won't be able to make it without the help and support from all of you.

First and foremost, I would like to express my deepest gratitude to my advisor, Professor Shaya Fainman. He provided me with maximum freedom and ample resources to learn and explore throughout my PhD journey. During the hardest period of my life, he showed great empathy and offered me strongest support, helped me went through that difficult time. I feel lucky to have had Prof. Fainman as my PhD advisor—not only for his professional guidance and the academic resources he generously shared but also for the trust and respect I experienced as a member of the UNO group.

I would like to thank my committee members, Prof. Tzu-Chien Hsueh, Prof. Zhaowei Liu, Prof. Yu-hwa Lo, Prof. Saintillan David, and also Prof. Abdoulaye Ndao, it is a great privilege to work with you.

I would also like to thank my amazing colleagues; Dr. Shimon Rubin, Dr. Hani Nejadriahi, Dr. Alex Friedman, Prabhav Gaur, Vladimir Fedorov, Karl Johnson, Zijun (Jay) Chen, Dr. Dhaifallah Almutairi and Dr. Andrew Grieco, it is an honor and pleasure to work and get along with you.

Finally, I would like to thank my father, mother, uncle, aunt, grandma and all other family members back in China for their unconditional support.

Life is unpredictable, some random incident might permanently change your life, the only thing you can do is swallow it. Wishing everyone safety and good health.

Chapter 1, in part, is a reprint of the material as it appears in Advanced Photonics 4, no. 4 (2022) and Nature Communications 14, no. 1 (2023). The original publications have been re-arranged for clarity for the reader. The dissertation author is the first author of this paper, with co-authors Prabhav Gaur, Shimon Rubin, and Yeshaiahu Fainman.

Chapter 2, in part, is currently being prepared for submission for publication of the material with co-authors Vladimir Fedorov, Prabhav Gaur, Shimon Rubin, and Yeshaiahu Fainman.

VITA

2017 Bachelor of Science in Physics, Wuhan University, Wuhan, China

2019 Master of Science in Materials Science and Engineering, University of Pennsylvania

2024 Doctor of Philosophy in Electrical Engineering (Photonics), University of California San Diego

PUBLICATIONS

Chengkuan Gao, Prabhav Gaur, Shimon Rubin, and Yeshaiahu Fainman. "Thin liquid film as an optical nonlinear-nonlocal medium and memory element in integrated optofluidic reservoir computer." *Advanced Photonics* 4, no. 4 (2022): 046005-046005.

Chengkuan Gao, Prabhav Gaur, Dhaifallah Almutairi, Shimon Rubin, and Yeshaiahu Fainman. "Optofluidic memory and self-induced nonlinear optical phase change for reservoir computing in silicon photonics." *Nature Communications* 14, no. 1 (2023): 4421.

Chengkuan Gao, Vladimir Fedorov, Prabhav Gaur, Shimon Rubin, and Yeshaiahu Fainman. "Polarization division multiplexing for photonic based physical reservoir computing" Opt. Express (In preparation for submission)

Gaur, Prabhav, **Chengkuan Gao**, Karl Johnson, Shimon Rubin, Yeshaiahu Fainman, and Tzu-Chien Hsueh. "Information Processing in Hybrid Photonic Electrical Reservoir Computing." *arXiv preprint arXiv:2404.01479* (2024).

Chaudhury, Sumilak, Karl Johnson, **Chengkuan Gao**, Bill Lin, Yeshaiahu Fainman, and Tzu-Chien Hsueh. "Micro-Ring Modulator Linearity Enhancement for Analog and Digital Optical Links." *arXiv preprint arXiv:2407.11172* (2024).

Alquliah, Amged, Jay Ke-Chieh Sun, Christopher Mekhiel, **Chengkuan Gao**, Guli Gulinihali, Yeshaiahu Fainman, and Abdoulaye Ndao. "Electrically Reconfigurable Non-Volatile On-Chip Bragg Filter with Multilevel Operation." *arXiv preprint arXiv:2408.10110* (2024).

ABSTRACT OF THE DISSERTATION

Physical Reservoir Computing in Photonics Integrated Circuit

by

Chengkuan Gao

Doctor of Philosophy in Electrical Engineering (Photonics)

University of California San Diego, 2024

Professor Yeshaiahu Fainman, Chair

Reservoir computing (RC) is a computational framework derived from Recurrent Neural Network (RNN), demonstrated advantage in time-series prediction and signal processing. Unlike traditional machine learning methods that rely on iterative weight optimization across the entire network, RC simplifies the training process by focusing only on a linear readout layer. This unique feature makes RC particularly attractive for applications requiring rapid adaptability, low computational overhead, and real-time data processing.

The heart of RC is the ‘reservoir’, which represents a high complexity, nonlinear system with short-term memory. The reservoir itself is typically a fixed structure, which can be treated as a ‘black box’ since the training happens outside the reservoir. So it is possible for a physical

system to be the reservoir, lead to the research in physical reservoir computing (PRC), which offer possibilities for ultra-high efficiency computation. A wide range of physical systems can serve as reservoir, among which, photonic systems stand out for their exceptional data transmitting speed, high bandwidth, and energy efficiency.

In this dissertation, we will present two PRC researches in photonic platform based on two different directions:

1. New physical reservoir system development.

We study a novel optofluidic silicon photonics system with self-induced phase change effect which relies on the coupling between geometric changes of thin liquid film and optical properties of photonic mode in waveguide, both theoretically and experimentally. The thin liquid film can operate as a nonlinear actuator and memory element, both residing at the same compact spatial region. The resulting dynamics allows to implement RC at spatial region which is approximately five orders of magnitude smaller compared to state-of-the-art experimental liquid-based system.

2. Performance enhancement in existing PRC system.

We investigate the potential of using Polarization Division Multiplexing (PDM) to enhance the performance of the photonic-based PRC system. Based on a Hybrid-Photonic-Electronic RC platform, we validate through simulation and experiments that PDM improves system performance by increasing the dimensions of the photonic reservoir. The results indicate decent performance improvements with minimum increase in system footprint, highlighting the potential of PDM as a scalable and efficient tool for photonic-based PRC systems.

INTRODUCTION

The rise of artificial intelligence (AI) is driving a new tech revolution in human society. Currently, photonics is accelerating this revolution with its terahertz (THz) level data transmission bandwidth and power efficiency in the form of photonic interconnects [1]. In the meantime, as most AI models are based on large-scale linear algebra operations, advances in new material system and fabrication technologies have enabled researchers to directly map artificial neural networks (ANN) algorithms onto photonic integrated circuits (PIC) platforms. This is achieved by performing matrix-vector multiplication (MVM) using photonic structures [2] such as Mach-Zehner interferometer (MZI) arrays [3] or wavelength division multiplexing (WDM) micro-ring resonator (MRR) arrays [4].

Apart from performing matrix multiplications in PIC, researchers have also utilized other properties of photonic circuit to realize additional functions for neuromorphic computing. For example, pulsed optical sources and novel phase change materials can be utilized for spiking neural networks (SNN) [5], diffractive gratings can be used for large scale data or weight encoding [6], on-chip optical delay line could serve as memory elements for reservoir computing (RC) [7]. Among these approaches, RC is receiving attentions due to its unique training methodology and network structure.

Currently, gradient decent is one of the most widely adopted method for training neural networks. However, implementing this method in a photonic system is challenging due to the intrinsic difficulty of backpropagating light field in real photonic circuits. So most of the optical neural network (ONN) studies rely on training the network by modeling the photonic system in digital computers, and then perform backpropagation algorithms [8][9][10]. While fully offline modeling of an ONN system becomes increasingly challenging as the network size keep

increasing and involve more errors. Although researchers have demonstrated several on-site training methods such as in-situ backpropagation by physically switching the forward and backward ports [11] or perform advanced fully forward mode (FFM) training method [12], not all ONN systems are capable of adopting such techniques.

Reservoir computing was originally a framework derived from recurrent neural network (RNN) which typically use more complex network with feedback loops as 'memories' in the system. These networks are often computationally expansive to be trained through direct fine-tuning of inside weights. Instead, RC simplify the training process by applying a simple linear fitting layer after the network output. This approach allows the complex network to be treated as a 'black box', enabling a physical system with inherent nonlinearity and short-term memory to be treated as a reservoir for RC. This methodology has driven studies on physical reservoir computing (PRC), which leverages the unique dynamics of physical systems to perform computational tasks [13][14][15][16][17].

In this dissertation, we present our PRC researches in two different directions:

In Chapter 1, we will discuss the study of a novel optofluidic system as a new potential physical platform for PRC. The basic optofluidic system can be conclude as a photonic waveguide with thin liquid film cladding, where a small metal patch is placed on top of the waveguide as localized heater. The heat generated from optical field will change the geometry of the liquid-air interface by thermocapillary effect. The change in liquid geometry will in-turn change the photonic mode inside the waveguide, result in complex dynamics. We will present:

- Theoretical formulation of the numerical simulation model we used to simulate the optofluidic system which require coupling between wave optics, fluid dynamics, and heat transfer.

- Simulation results of different photonic structures based on the basic model, demonstrate self-induced nonlinear phase change, nonlocal phase change, and transmittance change based on Bragg grating structures.
- Experimental realization of the proposed optofluidic system, including the optofluidic characterization setup which enable optical phase change measurement, photonic chip design and fabrication, and novel femtoliter droplet deposition technique.
- Experimental characterization result of self-induced nonlinear optical phase change effect, self-induced nonlocal optical phase change effect, and system modulation capability.
- Numerical and experimental demonstration of basic RC tasks.

In Chapter 2, we will study using polarization division multiplexing (PDM) to enhance the RC performance of an existing photonic PRC system by increasing the dimensions of the reservoir space. We will present:

- The Hybrid-Photonic-Electronic Reservoir Computing (HPE-RC) system we used as our PRC performance test platform.
- Experimental setup and numerical modeling of polarization division multiplexing (PDM)
- RC performance enhancement by PDM

Chapter 1 - Optofluidic memory and self-induced nonlinear and nonlocal optical phase change for reservoir computing in silicon photonics

1. Background

Light-matter interaction resides at the core of advancing our understanding of both light and matter properties. Emergence of robust integrated photonic platforms over the last two decades, characterized by miniaturized cross-section and higher refractive index contrast, were leveraged to enhance the optical intensity thus achieving nonlinear response of various matter degrees of freedom.

Exploring novel light-matter interaction regimes is fundamental to our ability to advance our understanding of both light and matter properties and to introduce novel technological capabilities. While light-solid interaction on the nanoscale attracted prime attention due to advancement of nanofabrication methods, enabling to observe numerous nonlinear optical effects in integrated photonics platforms [18][19][20][21], exploring light-liquid interaction remains an attractive research direction due to liquids' extremely rich phenomenology and transport regimes. In particular, since liquids allow molecular transport at the cost of relatively low energy compared to thermal energy in solid, it can support a variety of physical effects which are inherently not possible in solid system, such as optical solitons due to the reorientation of liquid crystal molecules [22], light branching in liquid films [23], light-induced tuning of plasmonic resonances [24], as well as modern extreme UV laser systems [25] with applications in high-resolution lithography. In this chapter, we explore the potential of light-liquid interaction in information processing.

we employ the previously theoretically proposed light-liquid nonlinear and nonlocal interaction mechanism [26][27], where localized light-induced heating invokes thermocapillary

(TC) [28][29][30] driven deformation of optically thin gas-liquid interface [31], to predict and characterize a set of new nonlinear-nonlocal effects in optofluidic integrated photonic components, and then leverage these effects to achieve RC capabilities. Fig.1 presents schematic illustration of the typical setup where the optical mode which propagates in the WG covered with thin liquid film, invokes heating in a small metal patch on the top facet of the WG due to optical absorption, leading in turn to TC effect and to liquid deformation. In case the liquid film is sufficiently thin, liquid deformation modifies the overlap of the evanescent tail with the gas phase above the liquid film, leading to self-induced change of optical mode properties such as phase or coupling coefficient to another WG, which we will discuss below.

2. Theoretical formulation of the COMSOL numerical simulation model

For numerical simulations we define silicon (Si) or silicon-nitride (SiN) channel waveguide (WG) designed to carry single mode at wavelength 1550 nm (we consider TM polarization), which is buried in silica (SiO2) layer in order to provide a flat surface for more straightforward numerical implementation. Our extensive 3D numerical analysis which takes into account the full dynamics of various degrees of freedom, allows quantitative analysis beyond previous studies which considered limiting assumptions such as small liquid deformation and effective 2D approximation schemes of surface plasmon polariton [26] and slab WG modes [27]. In particular, our simulations include intricate coupling where optical dissipation in the gold patch on top of the WG leads to Joule heating generation and its transport to gas-liquid interface; the latter triggers surface tension gradients along the gas-liquid interface which in turn invokes TC flow accompanied by liquid's thickness change above the active WG (Fig.1b) (in our terminology active WG accommodates gold patch whereas passive WG does not). For the simplest case of a single active WG the corresponding deformation of the dielectric cladding

leads to a self-induced change of the accumulated optical phase thus constituting a two-way interaction where the optical mode affects itself through the liquid, provided the gas-liquid interface overlaps with the evanescent tail. Furthermore, substantial in-plane spatial scale of liquid's indentation allows to achieve the so-called optical nonlocality where the active optical mode affects the passive optical mode even if the passive WG is displaced from region of maximal optical intensity.

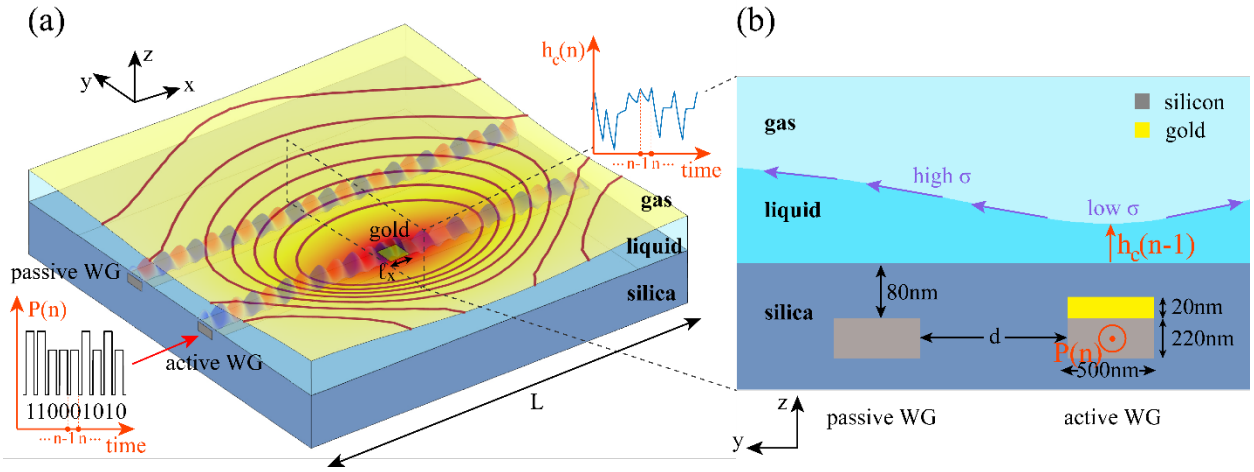

Figure 1: (a) Schematic description of the key components in the integrated optofluidic system under study describing the underlying mechanism of the light–liquid interaction and the memory used for RC. (a) 3D perspective presenting a box-shaped liquid cell of length L = 10 μm bracketed by vertical silicone walls, and an active Si channel WG on a silica substrate covered with a gold patch of dimensions $l_x \times l_y \times k$ enabling light-induced heating and subsequent heat transport to the gas–liquid interface, which in turn triggers surface tension gradients, represented by blue arrows in (b), leading to the TC effect and liquid film thinning. The latter leads to a self-induced phase change and/or to transmittance change in the single WG setup and also to a nonlocal effect, where the phase in the adjacent passive WG is modified due to liquid deformation. Darker colors on the liquid's surface in (a) correspond to higher temperature, whereas the dark red lines denote equal height levels. A sequence of high and low optical power pulses corresponding to logic "0" and "1", respectively. The finite relaxation time of the gas liquid interface allows us to employ it as a short-term memory, where the $(n-1)th$ pulse of power $P(n-1)$ induces $h_c(n-1)$ liquid thickness affecting the subsequent nth pulse of power $P(n)$. (b) 2D normal section, consisting of Si channel WGs of width w = 500 nm and height u = 220 nm buried in depth b = 80 nm under silica top surface and hosting a gold patch of thickness k = 20 nm and in-plane dimensions $l_x = l_y = 500$ nm; the initial liquid depth is $H_0 = 500$ nm.

To capture the complex coupling between light propagation, fluid dynamics, heat transport, and surface tension effects, we employed finite-element-based commercial software COMSOL Multiphysics [32] with Wave Optics, heat transfer, and CFD module, where changes of thin liquid film geometry are simulated by the moving mesh method. Since electromagnetic dynamics occurs on much shorter time scales compared to other processes we consider, the optical simulation is performed in the frequency domain, whereas all other processes are simulated in the time domain. For the WG and thinner gold patch, we use a free tetrahedral mesh resulting in 6×10^5 mesh elements and 4×10^6 degrees of freedom. These memory demanding simulations are performed on a constructed dedicated server with 16 cores and 512 GB memory; for instance, the single self-induced phase change simulation presented in Fig. 2 takes day scale simulation time.

Below we present the governing equations for the optical field, heat transport, fluid dynamics and the matching conditions across the gas-liquid interface. The coupling scheme between the four mechanisms operates as follows. First, the propagating optical WG mode interacts with a metal patch and induces heating which is then transported and triggers temperature gradient of gas-liquid interface, leading in turn to gradients of the surface tension. The latter invokes TC flows and thickness changes of the liquid film, leading to changes of the effective refractive index of the optical mode.

For optical field, Faraday and Ampere's law equations relating between electrical field $\vec{E}$, magnetic field $\vec{B}$, electric displacement $\vec{D}$, magnetic induction $\vec{H}$, and current density $\vec{J}$ are given by:

$$\vec{\nabla} \times \vec{E} = -\frac{\partial \vec{B}}{\partial t} \tag{1}$$

$$\vec{\nabla} \times \vec{H} = \frac{\partial \vec{D}}{\partial t} + \vec{J} \tag{2}$$

Applying $\vec{\nabla} \times$ operator on Eq (1) and employing: constitutive relation $B = \mu H$, Eq (2) and Joule's law $\vec{J} = \sigma \vec{E}$, yields:

$$\vec{\nabla} \times \left(\frac{1}{\mu_r} \vec{\nabla} \times \vec{E} \right) = k_0^2 \left(\varepsilon_r - \frac{i\sigma}{\omega \varepsilon_0} \right) \vec{E} \tag{3}$$

Here $k_0^2 = \omega^2 \varepsilon_0$, ε_0 and μ_0 are electric and magnetic vacuum permittivity; ε_r and μ_r are material electric and magnetic vacuum permittivity.

Heat diffusion transport is governed by:

$$\rho_m c_p \frac{\partial T}{\partial t} - \vec{\nabla} \cdot \left(k_{th} \vec{\nabla} T \right) = \vec{J} \cdot \vec{E} \tag{4}$$

Where T is temperature filed, ρ_m, c_p, k_{th} are the corresponding material density, specific heat and heat conductivity, $\vec{J} \cdot \vec{E}$ is Joule heat source term.

Dynamics of a Newtonian, non-compressible fluid in cartesian coordinate system is governed by the Navier-Stokes equations given by:

$$\rho \left(\frac{\partial u_i}{\partial t} + u_j \frac{\partial}{\partial x_j} \right) = \frac{\partial}{\partial x_j} \tau_{ij} + F_i \tag{5}$$

Where τ_{ij} is the corresponding energy-momentum tensor given by:

$$\tau_{ij} = -p\delta_{ij} + \mu e_{ij}; \quad e_{ij} = \frac{\partial u_i}{\partial x_j} + \frac{\partial u_j}{\partial x_i} + \frac{2}{3} \delta_{ij} \frac{\partial u_l}{\partial x_l} \tag{6}$$

Here u_i, F_i, ρ, p and μ are the fluid velocity components, body force components, density, pressure, and dynamic viscosity, respectively. The indices i, j, l run over three Cartesian coordinates x, y, z and summation convention over repeated indices is employed.

The interfacial Stress Balance Equation (SBE) which holds on the gas-liquid interface, is given by the following matching conditions:

$$\hat{n}_j \cdot \left[{\tau_{ij}}^{(2)} - {\tau_{ij}}^{(1)}\right] = \sigma \hat{n}_i \frac{\partial \hat{n}_j}{\partial x_j} - \frac{\partial}{\partial x_j} \tag{7}$$

Which in vector notation takes the form of:

$$\hat{n} \cdot \left(-pI + \mu\left(\vec{\nabla}\vec{u}^T + \vec{\nabla}\vec{u} - \frac{2}{3}\vec{\nabla}\cdot\vec{u}\right)\right) = \sigma\hat{n}\left(\vec{\nabla}\cdot\hat{n}\right) - \vec{\nabla}\sigma \tag{8}$$

Normal stress balance and tangential stress balance are obtained by projecting SBE on $\hat{n}$ and $\hat{t}$, which are given by:

$$\hat{n} \cdot \left(-pI + \mu\left(\vec{\nabla}\vec{u}^T + \vec{\nabla}\vec{u} - \frac{2}{3}\vec{\nabla}\cdot\vec{u}\right)\right) \cdot \hat{n} = \sigma\left(\vec{\nabla}\cdot\hat{n}\right) \tag{9}$$

$$\hat{n} \cdot \left(-pI + \mu\left(\vec{\nabla}\vec{u}^T + \vec{\nabla}\vec{u} - \frac{2}{3}\vec{\nabla}\cdot\vec{u}\right)\right) \cdot \hat{t} = \sigma_T \nabla_t T \tag{10}$$

Where in the last line we used $\hat{t}\cdot\vec{\nabla}\sigma \equiv \nabla_t\sigma$ and assumed the commonly employed linear dependence of surface tension on temperature $\sigma(T) = \sigma_0 - \sigma_T(T - T_0)$, σ_0 and σ_T are positive constants for the liquid-gas interface, here we use $\sigma_0 = 10^{-3}N/m$, and $\sigma_T = 10^{-4}N/m$.

Table 1: parameters used in the numerical simulation

	Gas	Liquid	Si	SiO_2	Gold	SiN
Thermal conductivity, k_{th} [W/(m·K)]	0.026	0.15	130	1.38	310	30
Density, ρ [kg/m^3]	1.2	930	2329	2203	19300	2500
Constant pressure heat capacity, c_p [J/(kg·K)]	1005.5	1500	700	703	125	170
complex refractive index, n + i·k	1	1.444	3.4757	1.444	0.5240+ 10.472i	2
Dynamic viscosity, μ [Pa·s]	1.8x10^{-5}	0.1	/	/	/	/
Ratio of specific heats, c_p/c_V	1.4	1.5	/	/	/	/

We use Dirichlet boundary conditions of fixed room temperature 20°C on the boundary for heat transport, Navier boundary conditions on the vertical walls and vanishing slip velocity

conditions for the liquid dynamics and PML boundary conditions for wave optics. Table 1 specifies the numerical values employed in the simulation, all parameters are at room temperature, 1 atm and for wavelength 1550 nm.

3. Simulation result

a) Nonlinear self-induced phase change

Consider a single Si channel WG with integrated gold metal patch, covered with thin liquid film described in Fig.2a. Following the mechanism described above, the metal patch serves as an optical heater which induces TC-driven flows and deformation of the liquid dielectric film. In our simulations we set liquid properties close to silicone oil which is an optically transparent and highly non-volatile liquid thus appropriate for future experimental realizations.

Figure 2(a) presents simulation results of the self-induced phase change effect due to the TM mode propagating in a single active WG covered with a thin liquid dielectric film of the initial thickness of 500 nm. In particular, Fig. 2(a) presents the corresponding deformation and temperature field of the gas–liquid interface at time t = 20 ms after the 0.1 mW continuous wave (CW) mode began to propagate in the WG, whereas Fig. 2(b) presents the gas–liquid deformation as a feedback response (circular arrow), allowing us to store information and affect subsequent optical pulses at the same compact spatial region without the need of dedicated large footprint optical feedback elements, e.g., optical rings [33]. The colormap describes electric field intensity at t = 20 ms and thin liquid-deformation along the x–z plane, where x is the propagation direction; note the effect of light reflection from the gold patch leading to distortion of the incoming mode. Figure 2(c) presents the electric field intensity at two different times along the planes x = −4.5 μm, x = 0 μm, and x = 4.5 μm, where x = 0 μm is the center of the gold patch.

Specifically, the images at the first row indicate that at t = 0 ms, i.e. prior to liquid film deformation, the incident TM mode experiences reduction in intensity but preserves its TM polarization. However, once the liquid film begins to deform, the second row indicates that after 20 ms the incident mode changes its shape due to superposition with the reflected wave from the gold patch, and the transmitted mode is no longer top-bottom symmetric.

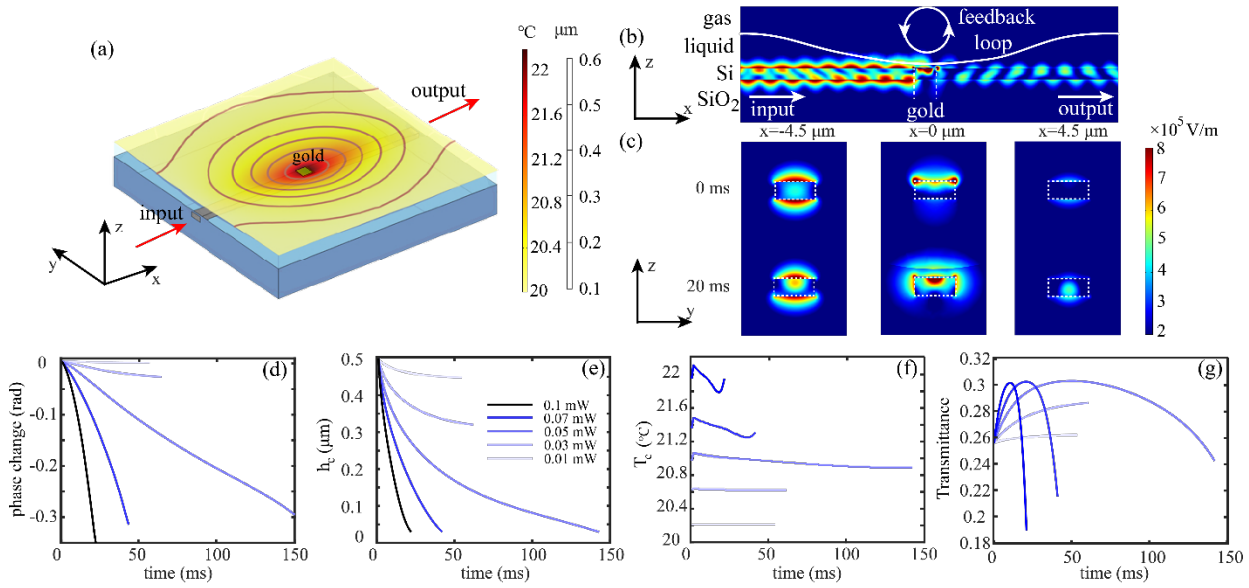

Figure 2: Numerical Multiphysics simulation results presenting self-induced phase change in a single active WG covered with a thin liquid film. (a) Deformed gas–liquid interface under 0.1 mW CW light-induced TC effect at time t = 20 ms (where t = 0 s is the time moment when the optical mode began to propagate) and (b) graphic representation of the internal optical-generated feedback (circular arrow) due to deformation of the gas–liquid interface, allowing us to invoke transient dynamics serving as memory storing the previous optical pulse and using the dynamics to affect the deformed profile and the optical pulse at the next time moments at the same actuation region. The colormap describes electric field magnitude along the x–z plane at time moment t = 20 ms; the gold patch resides on the top facet of the WG, and its dimensions along the x-axis are bracketed by the white dashed lines. (c) Electrical field magnitude along the normal section y–z at x = −4.5 μm, x = 0 μm, and x = 4.5 μm corresponding to left, central, and right columns, respectively, under 0.1mW incident intensity; first and second rows correspond to mode profiles at initial time t = 0 ms and t = 20 ms, respectively. (d) The corresponding phase change as a function of different optical powers in the WG due to (e) liquid film thickness change, where h_c is liquid thickness above the center of the gold patch. (f) The underlying change of the average temperature of the gold patch, T_c; (g) the corresponding transmittance as a function of time.

Figures 2(d)–2(g) present the self-induced phase change, deformation of the thin liquid film above the gold patch center $h_c(t)$ (i.e., at region of minimal thickness just above the center of the gold patch), average temperature of the gold patch $T_c(t)$, and the corresponding transmittance as a function of time, respectively, under various optical powers. Naturally, increasingly higher power levels and accompanying temperature gradients lead to more significant $h_c(t)$ and the corresponding self-induced phase change effects. Interestingly, at optical powers of 0.1, 0.07, and 0.05 mW, the corresponding liquid film deformation also induces prominent transmittance change, leading to a power reduction by approximately a factor of 2/3, which we attribute to impedance mismatch created by the liquid deformation. Notably, owing to the relatively low power levels required to activate TC-driven film thinning as well as the large refractive index contrast across the gas–liquid interface, sufficiently thin liquid film with high overlap of the evanescent optical tail with the gas phase supports a few orders of magnitude higher self-induced phase change compared with that of the thermo-optical (TO) effect. It is worth mentioning that due to the moving mesh method employed in COMSOL, the simulation terminates once the gas – liquid interface reaches the few elements thick film, as measured from the bottom of the liquid cell, leading to a phase change of ~0.3π rad.

In experimental realizations, which are not subject to such limitation, we expect to obtain even higher values of self-induced phase change and nonlocality scales, as well as self-induced transmittance/reflection modulation, shortly described below. Furthermore, given the fact that liquid deformation is mainly concentrated around the compact gold patch, based on our study, the size of the liquid cell can be, in principle, reduced to 2 μm, whereas higher values of self-induced phase change can be achieved by placing several gold (or other metal) patches along the WG.

b) Nonlocal effect

Consider the optofluidic components schematically presented in Fig. 3 and analyze the effect of the self-induced TC-driven deformation on modes in the two WGs as a function of their distance d. In particular, we consider close and far separation regimes characterized by $d < L_e$ and $d > L_e$, respectively, where L_e is the corresponding evanescent scale of the TM mode. To investigate the close separation regime, we focus on the directional coupler geometry with minimal distance d = 400 nm presented in Figs. 3(a) and 3(b), whereas in the far separation regime we consider parallel WGs geometry presented in Figs. 3(d) and 3(e).

Figure 3(c) shows the simulation results of the TM mode injected only into the active WG, indicating a decrease of the coupling coefficient as a function of liquid deformation, leading to decreased (increased) transmittance of the TM mode through the passive (active) WG as a function of time. In case the distance between the WGs is several microns (d = 1, 2, 3 μm), we can increase the nonlocal effect of the active WG on the passive WG by increasing the transverse dimension of the gold patch l_y, which facilitates more efficient heat transport and enables liquid film deformation profile, which extends toward the passive WG. This approach also allows us to alleviate the simulation limitation taking place due to its termination once the liquid film reaches a thickness of a few elements.

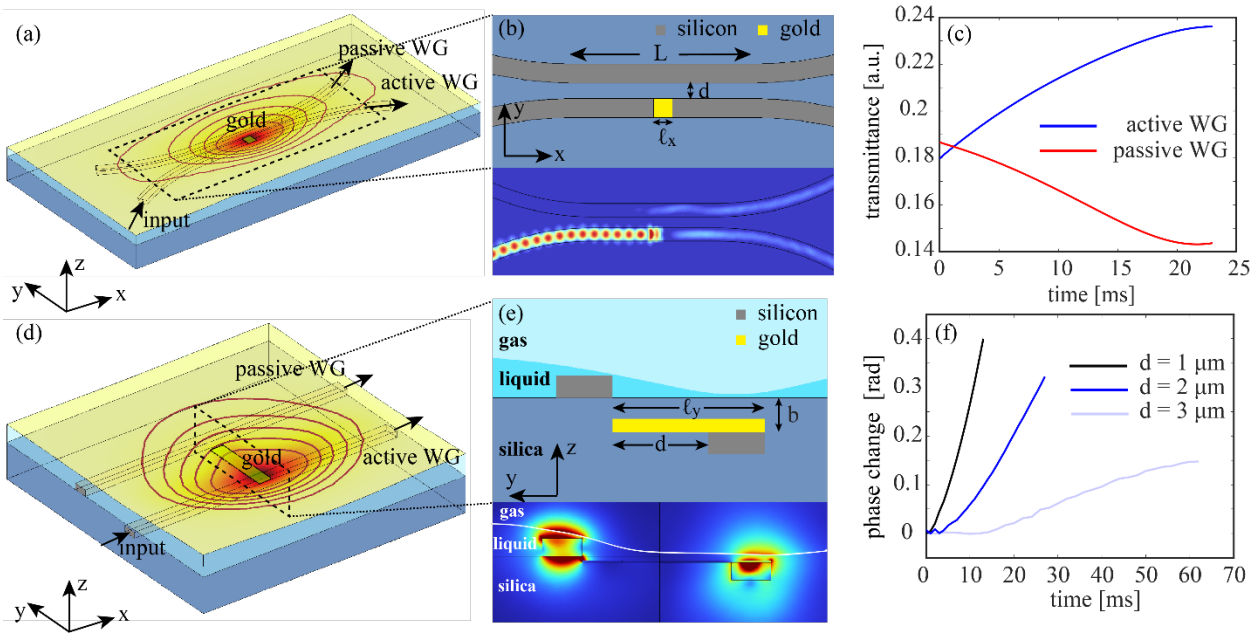

Figure 3: Numerical results demonstrating self-induced nonlocal interaction between two adjacent WGs in (a)–(c) the close and (d)–(f) far separation regimes, due to continuous TM mode of wavelength 1550 nm injected to the active WG leading to TC-driven deformation of the liquid film; geometric parameters of WGs and the gold patch are provided in Fig. 1. (a)–(c) Close separation regime with directional coupler geometry of d = 0.4 μm and interaction length L = 4.7 μm. (a) Temperature field and the geometry of the gas–liquid interface at time t = 23 ms under 0.1 mW; (b) top view of the WGs with the gold patch of longitudinal dimension l_x = 0.5 μm and the corresponding optical field at t = 23 ms; (c) numerical simulation results of optical intensity change in both WGs as a function of time. (d), (e) Far separation regime presenting three cases of parallel WGs separated by distances d = 1, 2, 3 μm and corresponding gold patches of lateral dimensions l_y = d þ w. (d) Temperature field and the topography of the gas–liquid interface at time t = 27 ms under 0.1 mW for the case d = 2 μm; (e) side view of the WGs with an elongated gold patch along the transverse direction, l_y , to facilitate heat transport from the active WG to passive WG and numerical results of two simulations at time 27 ms, where the mode is injected into active or passive WGs, indicating that the gold stripe does not support propagation of surface plasmon polaritons between the WGs. (f) Phase change in the passive WG mode as a function of time, for three different distances from the active WG.

Fig.3(d) presents 3D thin liquid film deformation and the underlying temperature map for the d = 2 μm case, whereas Fig.3(e) presents a normal cross section with the computational result of the corresponding modal structure. In particular, the latter presents numerical results at time t = 23 ms of two different simulations when the light was injected into the active or passive WGs and indicates that the gold patch does not guide surface plasmon polaritons from one WG to

another. Figure 3(f) presents the associated phase change in the passive WG as a function of time for three different separations, naturally indicating smaller values of phase shift for increasingly larger separations. Note that in contrast to the close separation regime, an initially low power (which is not sufficient to deform the liquid film) optical TM mode was also injected into the passive WG to analyze its evolution under the effect of the higher power mode in the active WG. Notably, the maximal separation between the WGs is much higher than the corresponding evanescent scale and also significantly exceeds other known optical nonlocality scales stemming from alternative optical nonlinearities, such as photorefraction [34], TO effect [35][36], and long range molecular interaction between liquid crystals molecules [37][38][39].

c) Self-induced transmittance and reflection in channel Bragg waveguides

Consider the SiN Bragg WG on silica substrate presented in Fig.4, where some of the ribs are covered with a gold patch of thickness k. Here, we employ SiN rather than Si because the former has a lower refractive index (2 at wavelength 1550 nm) leading to larger mode volume and thus to higher sensitivity of perturbations in the geometry of the gas–liquid interface. First, we design the periodic WG to admit a stop-band at a wavelength 1550 nm when it is covered with a thin liquid film of thickness 1 μm (as measured from silica substrate) and admit non-zero transmittance without the thin liquid film.

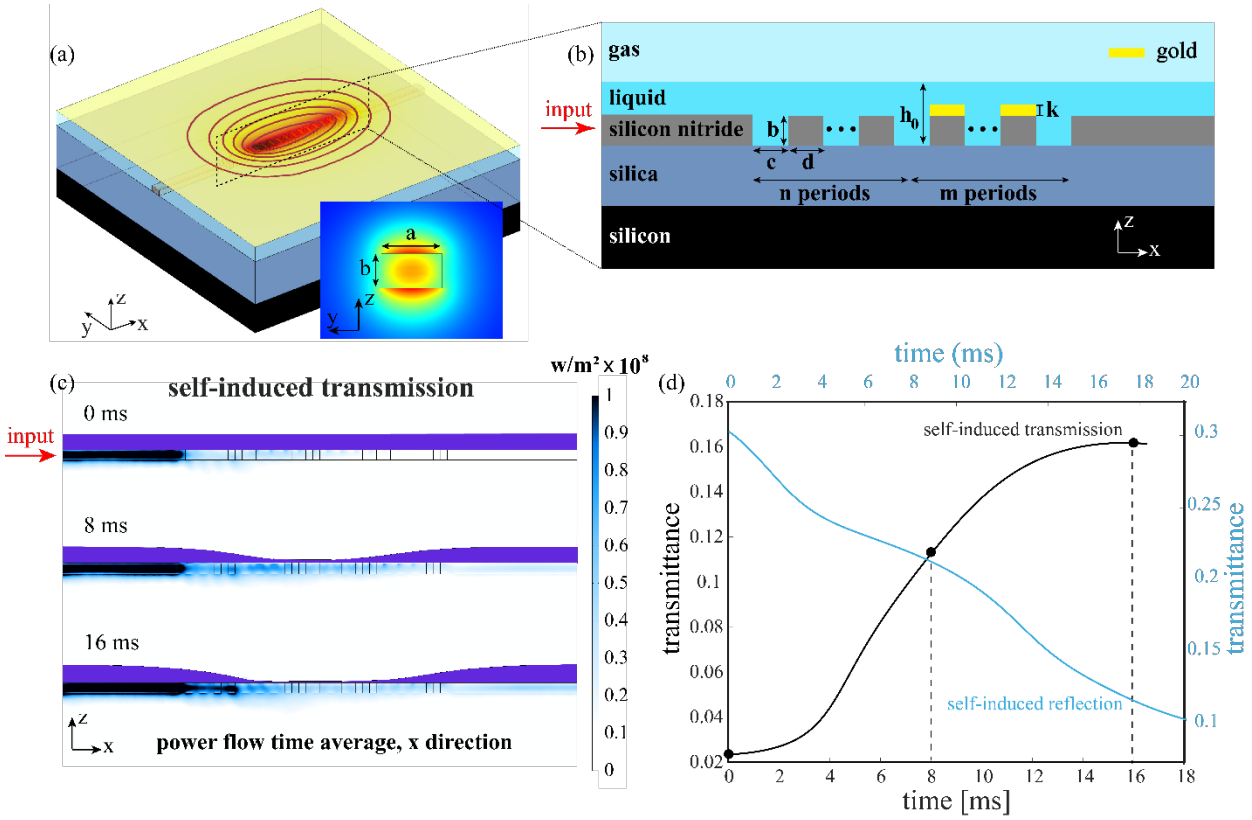

Figure 4: Numerical simulation results of the self-induced transmittance and reflection effects. (a) Presents the underlying 3D geometric setup of the periodic SiN Bragg WG on silica substrate, and (b) the corresponding 2D normal cross section in the x − z plane. Here, a = 0.7 μm, b = 0.4 μm, c = d = 0.2775 μm, k = 20 nm; number of ribs without gold patch n = 4 and with gold patch m = 15 for optimized performance. (c) Colormap of the corresponding power-flow along the WG, as a function of time. At successively later time moments liquid film over the periodic structure becomes increasingly thinner thus facilitating the optical propagation through the periodic structure designed to admit a stop band in the presence of liquid film. (d) Presents transmittance (black curve) as a function of time presenting also the transmittance values for thin liquid topography presented for the corresponding time moments in (c). The blue curve presents the decreasing function of transmittance for the complementary case of self-induced reflection where similar structure increasingly rejects light as liquid thickness approaches zero.

The evanescent penetration of the incident light a few periods into the SiN Bragg WG, which is inherent to stop-band conditions, triggers heating of the gold patches close to the input facet (left), which in turn triggers TC-driven deformation of the liquid film. As liquid thickness becomes thinner near the input facet, the designed propagation conditions facilitate deeper penetration of the optical mode into the periodic structure, thus leading to film thinning above

more distant regions from the input region, which in turn amplifies the process. Indeed, Fig. 4(c) presents an initially flat gas–liquid interface at t = 0 ms, liquid deformation with indentation closer to the input facet at t = 8 ms, and wider indentation over the central part of the periodic structure at the later time of t = 16 ms, leading to almost minimally thin liquid film above all WG ribs. Similarly, a periodic structure with slightly different period can be designed to support propagation once the WG is covered with liquid film and a stop band once the liquid film is replaced by air. Following the same arguments as above, self-induced liquid thinning over the periodic structure is expected to shift the propagation conditions and lead to lower transmittance, as indeed described by the blue curve in Fig. 4(d). Interestingly, the presented effects are reminiscent of electromagnetically induced transparency, which relies on a very different phenomenon, where quantum interference allows the propagation of light through an otherwise opaque atomic medium [40].

4. Details about experimental implementation

a) Photonic Young Interferometer for optical phase change measurement

Fig.5(a) schematically describes the experimental setup where CW laser source of wavelength 1550 nm couples optical TM mode from polarization maintaining lensed fiber into 220 × 500 nm Si channel WG by employing linear inverse taper. The optical phase changes are detected by employing photonic YI circuit, conceptually analogous to Young double slit experiment, where the coupled optical mode is split by using 50−50 Y-splitter [41] into active and passive WGs. In this circuit the active WG traverses the liquid cell whereas the passive WG serves as a reference and also admits gold patch (which does not interact with liquid) in order to balance losses allowing to increase visibility of the interference fringes formed upon emission into free space.

To form and capture the interference pattern as presented in Fig.5(a), we imaged the two output ports on a NIR CCD camera (Pembroke Instruments, 640X512 pixels, maximum 225 frames per second) by employing 50X objective (Mitutoyo, Plan Apo NIR) and 500mmlens together forming image system with 125 times magnification. We then slightly shifted the objective from the back focal plane in order to form interference fringes of the two point-like sources (output ports). By adjusting the shift allows to form three fringes in the image field.

Fig.5(b) presents schematic description of the normal cross section describing 1 μm long and 20 nm thick gold patch deposited on top facet of the active WG in order to dissipate light and operate as a localized heat source needed to trigger the TC effect. Since TM mode is characterized by stronger oscillation of the electrical field along the vertical z direction, it facilitates both more efficient optical dissipation on the metal patch and higher sensitivity in thickness changes of liquid film, compared to TE mode which admits oscillations mostly in the in-plane y direction.

The two output ports are set to a distance of 20 μm then produce interference pattern upon emission into the free space, and the optical phase change due to liquid perturbation in the active WG are then detected by measuring shift of the fringes with Charge-Coupled Device (CCD) camera. The relation between the shift of the objective from the image plane L, wavelength λ, the distance between two output ports d, and the fringe width W, can be determined by calculating the optical path difference in free space, given by $W = L\lambda/d$. By choosing $d = 20$ μm, $L \simeq 300$ μm, $\lambda = 1550$ nm, the corresponding fringe width on the front focal plane is $W \simeq 24$ μm. Since the objective and the lens form a 4f imaging system with 125 times magnification, the fringe occupies 125×24 μm $\simeq$ 3mm on the CCD sensor. The latter admits horizontal dimension of length 9.6 mm and therefore assuming the parameters above, the

sensor can accommodate three fringes, providing sufficient information on the fringes shift during the self-induced phase change.

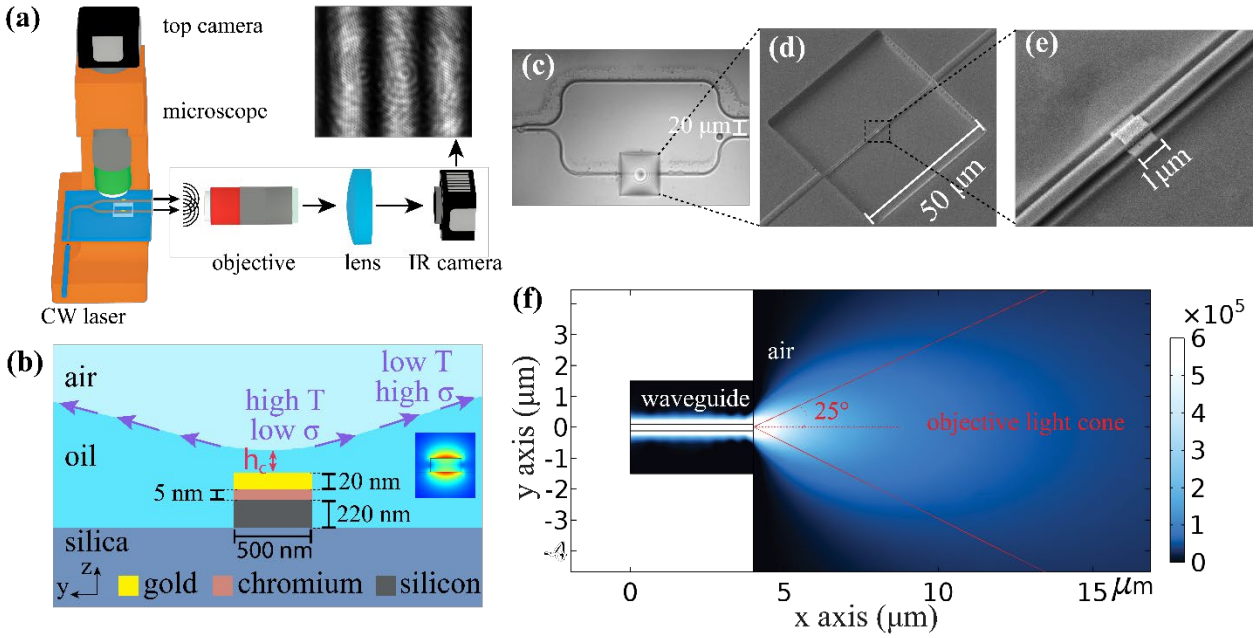

Figure 5: Key components of the optofluidic system and preparatory steps allowing to observe the self-induced phase change effect and its implementation for RC. (a) Schematic description of the experimental system allowing to couple continuous wave (CW) laser source of wavelength 1550 nm into SiPh chip, and detect interference fringes shift due to liquid deformation. (b) Schematic illustration of the normal section presenting 220 × 500 nm active WG, integrated 20 nm thick gold patch (with 5 nm thick chromium adhesion layer), as well as optically generated surface tension gradients triggering TC-driven thin liquid film deformation. The corresponding changes of the overlap of the TM mode with air leads to optical phase change and is detected by shift of interference fringes in the IR camera. (c) Top camera image of the photonic Young Interferometer (YI) circuit presenting: Y-junction, liquid cell of dimensions 50 μm×50 μm×3 μm hosting the active WG with liquid, and the 20 μm separated output WGs ports emitting into the free space. (d) SEM image of the etched cell in the thermal oxide cladding used as a liquid chamber. (e), Higher magnification of the SEM image showing the metal patch on top of the WG. (f) Optical simulation result presenting optical mode emitted from WG into the free space, and the spatial region corresponding to NA of the objective collecting the optical power. The latter is approximately equal to 28%.

We also estimate the optical power in the active/passive WG by consider several loss mechanisms. Based on our measurement results in a single bare WG without liquid cell and without gold patch, under best fiber-chip coupling condition, 1 mW input laser power (before coupling into the chip) yields 50 μW after the 0.42 NA objective lens, which collects the light in

a light cone with a $\sim 50^{o}$ apex angle, as shown by the red curve in Fig.5(f). By a frequency domain wave optics COMSOL simulation which simulates WG emits TM polarized light into free space, we can get the optical power intensity distribution as shown in the color map. From this simulation, approximately 28% of optical energy sits inside the light cone. Furthermore, the transmittance of the objective is 60% @1550 nm, the impedance mismatch for TM mode (effective index 1.7) yields another 10% loss, hence combining with the above, and assuming negligible propagation loss in silicon WG, we estimate fiber-to-chip insertion loss to be $10log10\left(\frac{50}{1000\times0.9\times0.28\times0.6}\right) \cong -5\ dB$. Consequently, the WG power PWG can be related to input power P_I via $P_{WG} = P_I/6$ where additional factor of two stems from splitting of the input WG into two WGs.

b) Chip fabrication

The silicon photonic chip was fabricated by the Applied Nanotools INC foundry. The WG patterns were defined by electron beam lithography (EBL) and reactive ion etching (RIE) processes on a Silicon-on-insulator (SOI) wafer with a 220 nm thick Si device layer, a 2 μm thick buried oxide layer and 725 μm thick silicon handle wafer. Afterwards, the gold patch was defined by optical maskless lithography (MPL) + magnetron sputtering lift-off and a 3 μm thick SiO2 cladding was deposited using chemical vapor deposition (CVD). In order to create windows in the oxide cladding serving as liquid cell, the pattern was first defined by MPL, and then RIE was used to etch approximately 2.5 μm oxide layer in order to protect the WG structure. The remainder of 0.5 μm thick oxide layer was removed by diluted Buffered Oxide Etch (BOE). Fig.5(c-e) presents optical and SEM images of the photonic circuit, the etched box-shaped cell with the WG and the gold patch on top of the WG, respectively.

c) Femtoliter liquid droplet deposition method

Crucial for our ability to conduct repeatable and controlled experiments, is to deposit into the etched cell silicone oil droplets of volume of few femtoliters. Since development of femtoliter droplet deposition methods is still an active field of research [42][43], we employed triboelectric effect in order to trigger electrostatic-based silicone oil drop-by-drop emission from glass tip to silica substrate, where the emission rate is controlled by modifying the distance between the tip and the silica substrate. Silicone oil (PHENYLMETHYLSILOXANE (cas number 9005-12-3, refractive index 1.444), Gelest®) was deposited into the etched liquid cell by employing the triboelectric effect known to invoke electrostatic charges in dielectric materials by scrubbing glass tip (Schott Duran borosilicate glass pipette, World Precision Instruments®) with nitrile gloves.

The electrostatic charges in turn led to electrohydrodynamic atomization (a.k.a. electrospray) [44] of femtoliter silicone oil droplets without the need to employ external electrodes. Fig.6(a) presents the preparatory step where the optical phase monotonically increases during droplet deposition process into the liquid cell; the insets describe four microscopy images of liquid's surface at corresponding moments of time. Fig.6(b) presents typical 3D profile of silicone oil surface, whereas Fig.6(c) provides height along cell's diagonal indicating that the film tends to wet the vertical sidewalls, enabling optically thin liquid film in the central region of approximate thickness 0.5 μm above the silica substrate. Topography of silicone oil film was achieved by employing white light interferometry system by Profilm 3D® (Filmetrics, San Diego, CA, USA).

The distance between the tip and silica substrate was few tens of microns, and controlling this distance affected droplet emission rate from the tip. Fig.6(d) demonstrates that for some

arbitrary initial location of the glass tip (estimated to be few tens of μm above the chip), further shift of the tip away from the chip decreases the deposition rate and increases the time needed to fill the cell.

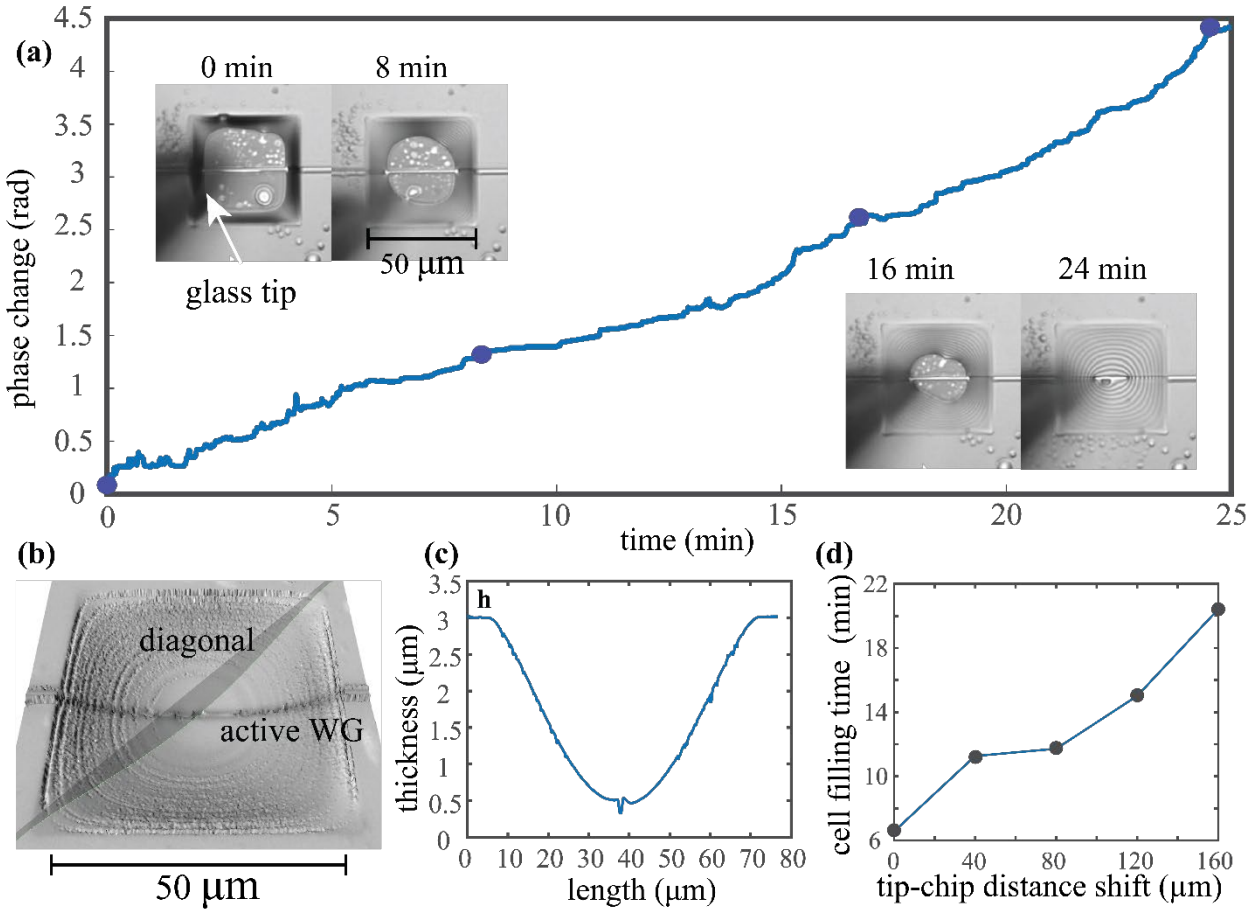

Figure 6: (a) Experimental results presenting phase difference between the two arms of photonic YI as a function of femtoliter droplet deposition process allowing to fill the etched cell with thin silicone oil film; top camera presents the liquid cell at specified time moments with purple disks indicating the corresponding phase change values. (b) 3D profiles of liquid surface measured by White Light Interferometry. (c) liquid thickness extracted from the 3D profile, indicating about 0.5 μm thick film in the center region of the liquid cell. (d) Experimental result indicating that tip-chip distance increase leads to increase of cell's filling time and hence to decrease of the deposition rate. In turn it signals that the origin of the deposition rate is electrostatic-based. The initial tip-chip distance is unknown and estimated to be few tens of μm.

5. Experimental characterization of the optofluidic system

a) Optical phase change measurement and noise analysis

In our experiments, we detect the self-induced phase change effect due to liquid film deformation, by monitoring shift of the interference fringes. In order to determine the noise threshold, i.e., the minimal phase change triggered by modification of some physical parameter, we perform two types of measurements. First, we would like to determine the role of TC effect relative to the more traditional heat-based TO effect by comparing shift of interference fringes in case the liquid cell is filled with silicone oil to the case when the liquid cell remains empty, presented in Fig.7(a) and Fig.7(b), respectively, where solid curve is the raw acquired data obtained by taking the arithmetic mean of all rows, dashed curve is generated by applying the additional step of MATLAB's built-in 'smooth' function. Assuming that the distance between two adjacent peaks in the same curve is 2π, fringe shift due to TC-effect in case of 500 nm thick silicone oil is $2\pi \times 157/195 = 1.61\pi$. Similar measurement without liquid film presents phase shift of only 7 pixels. Since our field of view captures about three fringes and each fringe occupies approximately 200 pixels, the minimal resolution of the phase change measurement is around $2\pi/200 = 0.01\pi$ rad.

To understand whether the 7 pixels shift presented in Fig.7(b) is below or above noise threshold we perform second type of measurement presented in Fig.7(c) where active WG without liquid is exposed to oscillatory or constant optical power. The acquired data for the case of constant power described by central and bottom panels of Fig.7(c) over a span of 5 s for input power levels 1 mW and 22 mW, respectively, indicate that the acquired signal is subject to about two pixels natural fluctuations presumably due to mechanical vibrations, corresponding to 0.02π rad phase shift.

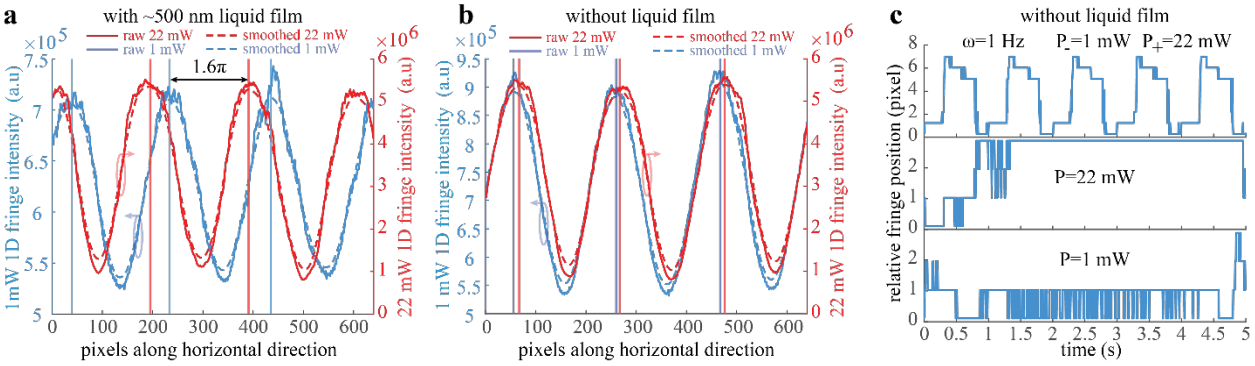

Figure 7: Experimental results analyzing: (a) interference fringe shift due to power increase from 1 mW to 22 mW, as a result of 500 nm thick silicon oil film deformation. (b) Reference case against (a) but with empty trench without silicone oil. (c) Location of single fringe peak as a function of time in case of 1 Hz input signal modulation (top panel), constant 22 mW (central panel), and constant 1 mW (bottom panel) all occurring without presence of liquid film.

For a device without liquid film, there should be no fringe movements apart from the random noise, but as shown in Fig.7(c), when doing a 1 Hz modulation between 1 mW and 22 mW without liquid film, around 7 pixels modulation depth is also monitored, which is not random and much higher than 2 pixels. This fringe movement may come from two parts, first is when changing the light intensity, the imperfection of our imaging system will shift the intensity distribution a little bit, causing some slight movement of the fringe peak location, as shown in Fig.7(b) which plots the raw and smoothed fringe curve, we can see that from blue curve to red curve, the left part of each fringe still matches, the fringes are more expanded rather than moved. The second possibility is thermal optical effect induced phase change.

b) Self-induced nonlinear phase change effect

Fig.8(a,b) and Fig.8(c,d) present experimental results of the self-induced phase change effect for approximately 0.5 μm and 1 μm thick silicone oil film, respectively, as a function of laser power modified in steps of ±0.25 mW. In particular, Fig.8(a) presents strictly increasing phase shift as a function of incoming optical power described by the red curve point 1-2-3-4,

whereas the regime with subsequently decreased optical power, which is dominated by ambient surface tension forces and relaxation of the invoked deformation, lead to phase change values along the blue curve point 4-5-6-1. Interestingly, the two curves enclose closed hysteresis loop which is typically observed in wetting experiments, and attributed to history dependent contact angle hysteresis and also to asymmetric advancing and receding film dynamics [45][46]. For instance, the latter can stem from either topographical features or chemical nonhomogeneity factors [47][48], which are both present in our photonic chip and are represented by Si channel ridge WG on silica substrate and the gold patch.

Top view microscopy images of the silicone oil under red LED illumination (central wavelength λ_{LED} = 680 nm) of corresponding configurations presented in Fig.8b, indicate that the transition from state 1 to state 2 is characterized by relatively small surface deformation and does not lead to film rupture. However, for optical power above 13 mW, the liquid film evolves towards ruptured state 3 and subsequently to state 4 with increasingly larger dewetted region, which is accompanied by higher slope of the phase change curve (compared to section 1 to 3) due to more significant overlap of air with the photonic evanescent tail. After each optical intensity change, we allowed at least 3 s relaxation time in order to allow the liquid film to reach its new static configuration.

Decreasing the optical power leads to reduction of the size of the dewetted region presented in state 4 to 6 of Fig.8(b), and for power level 8 mW the liquid film experiences collapse of the ruptured region and convergence towards the initial state 1 achieved at lower power values. Note that since the same laser source is used to excite the liquid as well as to form the interference fringes, some minimal non-zero optical power is initially required to circulate in both WGs. Our finite elements numerical simulation results (green dashed curve in the lower left

part of Fig.8(a)) present quantitative agreement against the experimental results in the pre-rupture regime 1 to 2, but is not capable of handling scenarios with ruptured film at higher optical power, due to limitation of the employed moving mesh method [15].

Fig.8(c) presents similar self-induced phase change effect and closed hysteresis curve for 1 μm thick silicone oil film, indicating that in this case the deformation stage prior to liquid rupture between state 7 and 8 introduces very small phase change value 0.04π rad, i.e. approximately order of magnitude smaller compared to the changes in the thinner film between the pre-rupture states 1 to 2. Smaller phase change values stem from larger distance between the WG and the gas-liquid interface, and therefore to less prominent overlap of the evanescent optical mode with the gas phase. Applying higher power of 12 mW triggers liquid instability leading to abrupt change of gas-liquid interface geometry from deformed configuration 8 to ruptured configuration 9 accompanied by significant phase change values 0.8π rad. Further increase of applied optical power leads to larger values of phase change between states 9 to 11 due to dewetting of the liquid film seen in Fig.8(c). Lowering the optical power leads to phase change evolution along the blue curve and small rupture healing between states 11 and 12. Around 8mW abrupt healing takes place accompanied by phase change of approximately 1.2π rad.

Importantly, while the maximal phase change reported above (Fig.2a) is approximately 1.7π rad, measurement under identical optical power without silicone oil yields values below noise level indicating that the relative magnitude of TC effect relative to TO effect is at least larger by a factor of 24 calculated by TO coefficient of Silicon [36].

It is worth mentioning that the hysteresis effect can be associated with memory and history dependent processes, however, as we will present in the following, the memory effect we employ

in this work for RC does not directly rely on hysteresis behavior, but rather on finite relaxation time of optically thin liquid film.

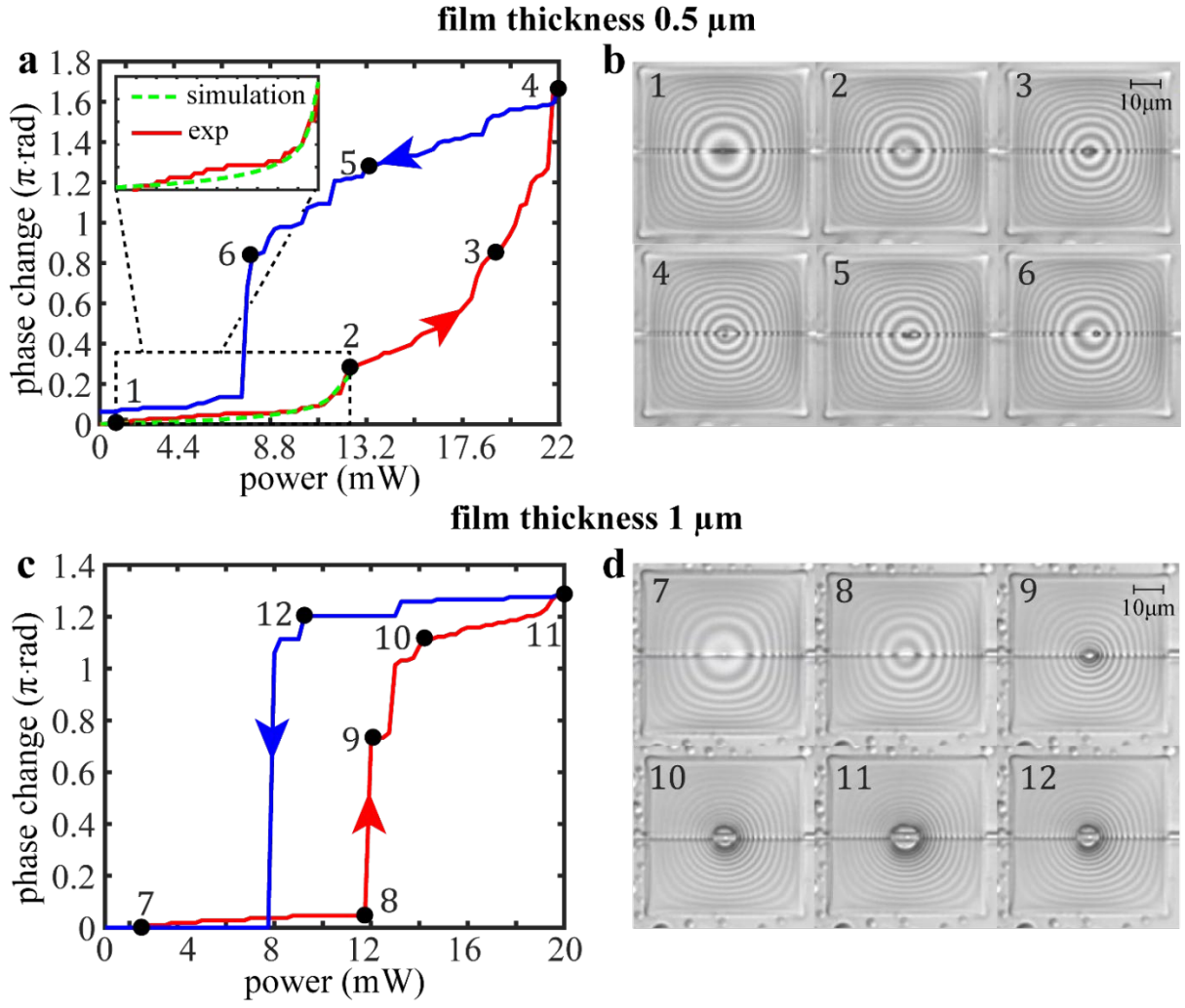

Figure 8: Self-induced phase change effect as a function of incident optical power for shallow and thick liquid films, measured by utilizing photonic YI circuit. (a,b) and (c,d) present experimental results of phase change as a function of the incident optical power in the active WG for 0.5 µm and 1.0 µm initial silicone oil thickness, respectively. Both cases admit gradual increase of the phase as a function of increased optical power (red curves) reaching to maximal values of 1.7π rad and 1.3π rad, and phase decrease as the power is decreased (blue curves) leading to hysteresis loop. (b) Top view optical images of the silicone oil cell corresponding to the parameters at the black points labeled between one to six on the curves presented in (a) and (b), where state 1 corresponds to initial configuration whereas state 2 to the configuration where the gas-liquid interface nearly touches the WG. Similarly, (c) presents hysteresis curve for 1 µm thick liquid film with more abrupt transition to ruptured state. Assuming normal incidence of the red LED source, and employing the condition for destructive interference $\lambda_{LED}/2n_{oil}$, we estimate the contact angle of the rupture in configuration 11 as approximately 5.5°.

c) Self-induced nonlocal effect

Fig.9 employ photonic YI similar to the circuit presented in Fig.5 but with two WGs in the liquid cell (see Fig.9(b)), strengthen the numerical results as mentioned in Chapter 1 section 2b. In particular, Fig.9(a) indicates that the liquid deformation triggered by the active WG first leads to positive phase change (①-③), but then as the indentation extends towards the passive WG the difference of optical paths is reduced leading to phase decrease (③-④ in Fig.3a). Fig.9(c) presents top view microscopy images of liquid film configurations at corresponding times ①-⑥ indicating that the deformation in configurations ③ and ④ indeed reaches the passive WG.

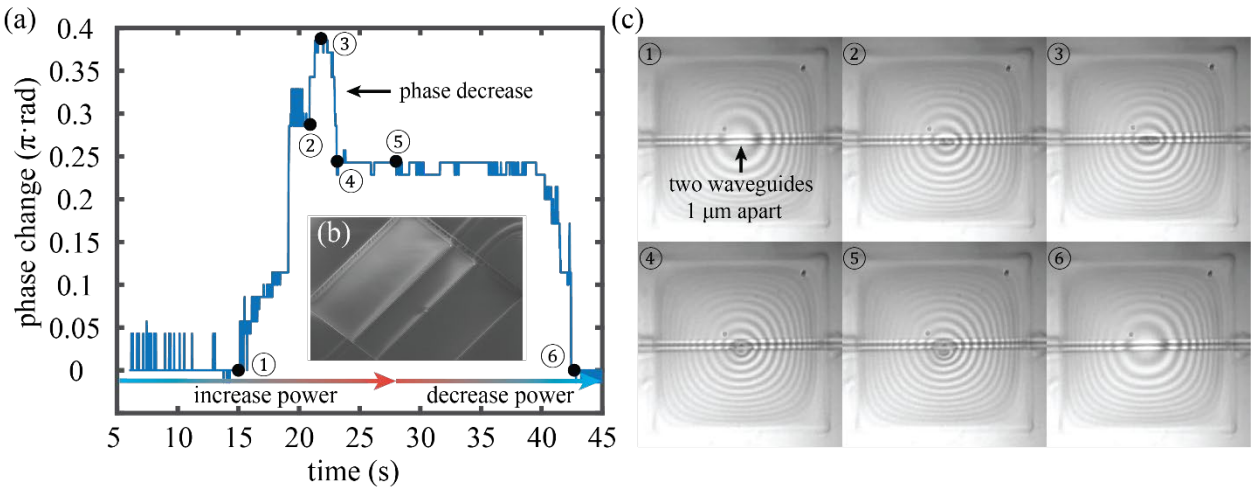

Figure 9: (a) Experimental results presenting evidence for optical nonlocality due to liquid film deformation in a system of two adjacent WGs separated by 1 μm. (b) SEM image of the liquid cell. (c) Top view microscopy images under λ=680 nm illumination describing ①-⑥ silicone oil configurations corresponding to labels near the phase change curve in (a).

d) Self-induced intensity change as a function of applied modulation frequency

Next, we consider photonic MZI circuit with a single output port, allowing to translate phase change into intensity change and employ a point detector capable to monitor dynamical processes of liquid deformation which evolve on sub microsecond time scale. First, we consider

DC regime, presented in Fig.10(a), where increasing input optical power leads to strictly increasing output power described by the red curve 13-14-15-16; subsequent decrease of input power leads to output power described by the blue curve 16-17-18-13 forming a closed hysteresis loop. Contrary to the YI circuit (Fig.8(b)) where fringes shift is already indicative of nonlinear response due to liquid deformation, changes of the optical power in in the MZI circuit can in principle also stem from changes of input laser power levels which are unrelated to liquid response. In order to discriminate between the nonlinear response due to liquid deformation and changes of input optical power, we subtract from the total measured power (P) the linear contribution of the input power (P_l), expressed as $P_{nl} = P - P_l$, which isolates the nonlinear contribution. Fig.10(a) presents experimental measurements in photonic MZI circuit where the total power P is described by solid red and blue lines whereas the nonlinear response P_{nl}, is described by blue and red dashed lines, where red/blue indicate increasing/decreasing optical power regime.

In particular, at power levels between 10 mW to 19 mW silicone oil film (approximate thickness 1 μm) experiences relatively small deformation (pre-rupture), captured by microscopy images 13 and 14, presented in Fig.10(b), and hence leads to a negligible nonlinear response represented by a practically flat red dashed line in Fig.10(a) in that power region. Nevertheless, for optical power levels above 19 mW the dashed line 14-15-16 is increasing, indicative of a nonlinear response due to liquid deformation. Similarly to the YI measurements reported in Fig.8, subsequent decrease of the input power yields strictly decreasing curve 16 - 18 enclosing a closed hysteresis loop with the red curve.

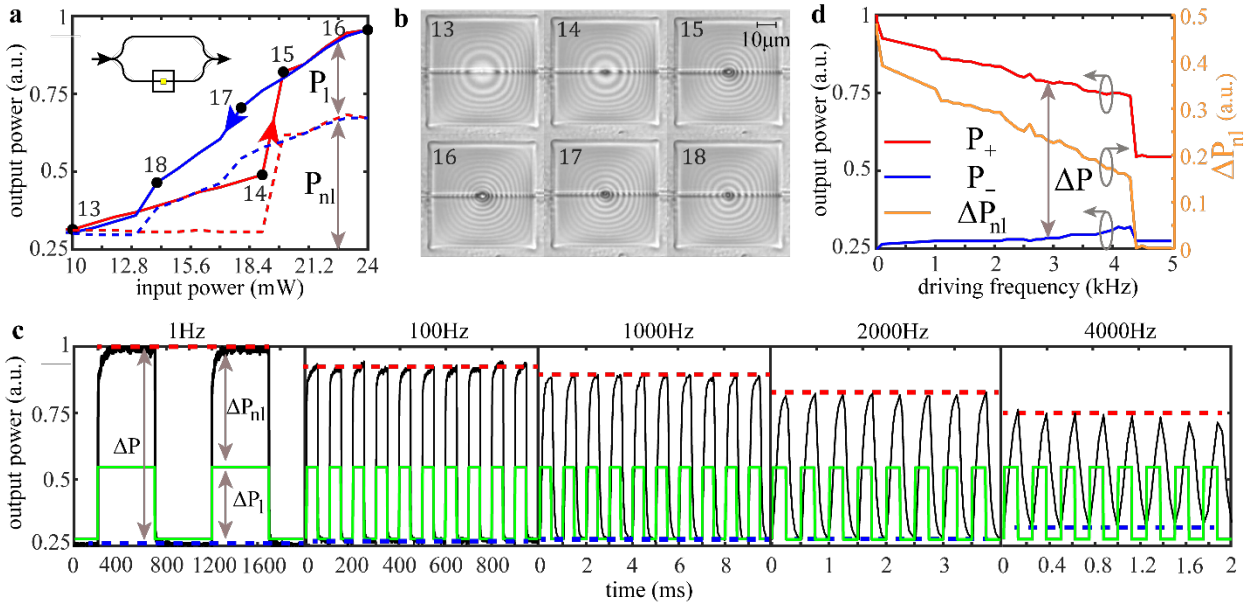

Figure 10: Self-induced phase change leading to intensity modulation as a function of input power and driving frequency in MZI circuit. a, Self-induced intensity change as a function of CW optical signal, due to optically induced deformation of liquid film of initial thickness of approximately 1 μm. The increment steps were of ±1 mW and with relaxation time between successive power levels approximately 3 s to allow sufficient relaxation into stable configuration. The dashed lines (P_{nl}) represent nonlinear output response obtained by subtraction of the corresponding input power (P_l) defined by Eq.1. **b**, Top view microscopy images of the correspondingly numbered states of the liquid film in **a**. **c**, Output signal as a function of time for representative frequencies 1 Hz, 100 Hz, 1000 Hz, 2000 Hz and 5000 Hz where the green and black curves represent the linear and nonlinear power response, ΔP_l and ΔP_{nl}, respectively. The red and blue lines represent the maximal (P_+) and minimal (P_-) values of Δn_l. The maximal and minimal power levels of the input signal (green curve) are 16 mW and 5.5 mW, respectively. **d**, P_+, P_- and ΔP_{nl} as a function of driving frequency ω, which are described by red, blue and green curves respectively.

Next, we consider the output power of the MZI circuit under the action of AC optical input signal as a function of driving frequency (ω) and liquid cell of the same thickness as in the DC case above. Fig.10© presents output power (black curve) due to square wave input optical power (green curve) for five different driving frequencies. We can define the nonlinear response function ΔP_{nl} as: $\Delta P_{nl} = \Delta P - \Delta P_l$; $\Delta P \equiv P_+ - P_-$, which eliminates changes of the input power and captures the nonlinear power response due to liquid deformation. Here, ΔP is the modulation depth of the output power, i.e. the difference between the maximal (P+) and the minimal (P−)

values of the output power described by the red and the blue dashed curves in Fig.10©, respectively, whereas ΔP_I is the fixed ω independent modulation depth of the input signal. Performing ω sweep over smaller steps, presented in Fig.10(d), indicates that ΔP and its nonlinear component ΔP_{nl}, are both decreasing functions of ω. Interestingly, ΔP_{nl} admits abrupt transition with nearly vanishing ΔP_{nl} above 4.3 kHz, indicative that the output and input signals are practically identical and hence implying that the liquid film does not respond under driving signals of sufficiently high ω, explicitly demonstrated by the 5 kHz case presented in Fig.10©. In fact, the latter could be anticipated from behavior of simpler mechanical systems such as forced damped oscillator, where the resultant amplitude decays as driving frequency tends to infinity.

6. Simulation and experimental result for Reservoir Computing

a) Simulation

i) Simplified 1D model and fading memory effect

To construct RC simulation, we employed the following three steps: (i) collected dynamics of $h_c(t)$ as a function of time for numerous driving optical powers and initial conditions; (ii) constructed reduced 1D model describing dynamics of $h_c(t)$ under first order ordinary different equation with power dependent coefficients; (iii) employed the reduced evolution equation to simulate dynamics of thin liquid film under driving optical sequence, collect the corresponding output data and then perform reservoir training and test its performance.

First, we employed ~100 3D simulations of the device we present in Fig.1 providing gas-liquid interface deformation & restoration under equivalent heat source assumption, as shown in Fig.11, which get rid of optical simulation and significantly reduce the computational cost of each model in terms of memory and computation time at the cost of introducing a small error.

Since under optical excitation the temperature reaches equilibrium on time scale of few microseconds (as we verified in the simulation), which is much smaller compared to time scales governing evolution of thin liquid film, introducing equivalent temperature source won't affect significantly liquid dynamics during microsecond time scale under continuous optical power. From simulation, the mean steady state temperature T in the gold patch versus input optical power P can be linearly expressed by: $T(K) = 15.75(K/W) \times P(W) + 293.15K$

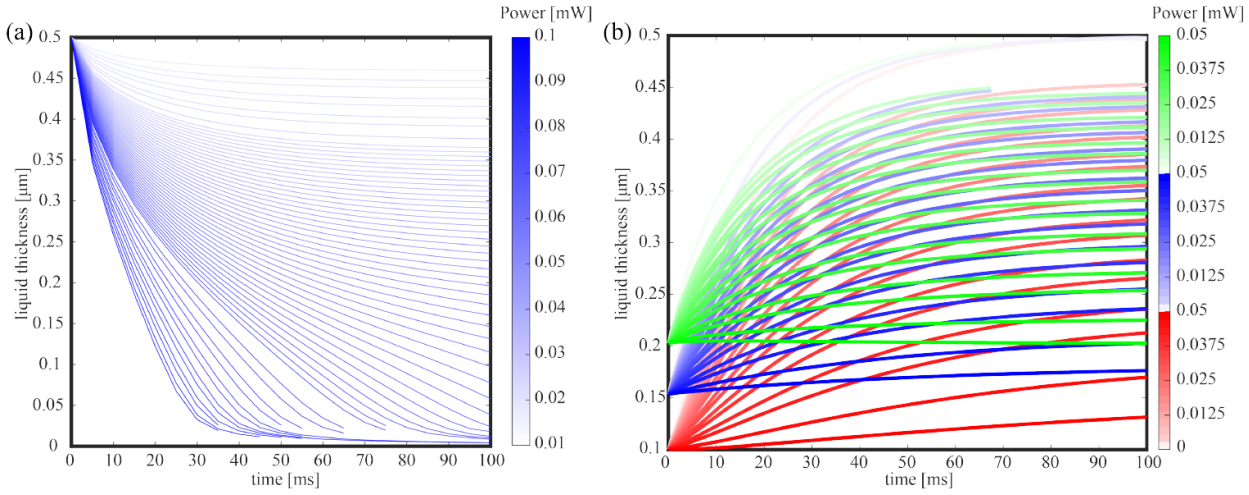

Figure 11: Numerical results presenting thickness of thin liquid film of initial thickness $h_c(0)$ = 500 nm at a central point above the gold patch as a function of time for various optical powers and various initial conditions. (a) Liquid film thickness as a function of time under approximately 65 different power levels in the range bracketed by 0.01 mW and 0.1 mW describing film thinning. (b) Liquid thickness $h_c(t)$ for initial conditions 0.1, 0.15, 0.2 μm; each liquid thickness corresponding to the initial conditions above is subject under approximately 15 different power levels in the range below 0.05 mW corresponding to film relaxation to thicker configuration.

In order to incorporate the numerous data curves presented in Fig.11 into a compact numerical model which allows prediction of $h_c(t)$ under various driving optical powers, we fit the data to the following first order ordinary differential equation:

$$\dot{h}_c(t) = \alpha(P)h_c(t) + \beta(P) \tag{11}$$

Here $h_c(t)$ is liquid thickness above gold patch center as a function of time t; P is a constant value of optical power carried by the WG; $\alpha(P)$ and $\beta(P)$ are power dependent coefficients explicitly given by: $\alpha(P) = 0.4368P - 0.0589,\ \beta(P) = -0.5546P + 0.0469$, which is presented in Fig.12(b). We then employ Eq.11 to predict liquid evolution $h_c(t)$ under power levels P and P/2 (corresponding to logical 'zero' and 'one') during time window τ_w, and zero power during τ_r. For each value of h_c we then employ the one-to-one relation between liquid thickness to corresponding phase change which is described in Fig.12(c). The fit (black curve) between the two quantities can be interpolated by $\Delta\varphi TC\ =\ 2.786 \times exp(-7.082 \times h)$.

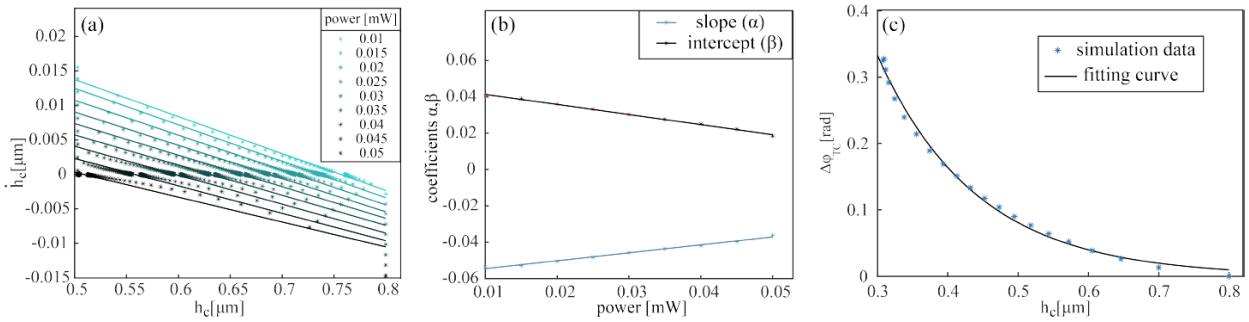

Figure 12: (a) Linear fit evolution in the phase space $(\dot{h}, h)$ for different power values together with a linear fit given by Eq.11. (b) Fitting of the coefficients α, β as a function of power. (c) The one-to-one relation between liquid thickness h_c above gold patch center and the self-induced phase change $\Delta\varphi TC$.

Now we can consider the reservoir dynamics. Assume power P maintains constant power levels on some time intervals, partition the total time period T into N arbitrary intervals at times $[t_0, t_1, \dots, t_N]$ of corresponding length $[T_1, T_2, \dots, T_N]$, where $t_N = T$. Also assume the liquid thickness at corresponding times is given by $[h_0, h_1, \dots, h_N]$. For any interval where the optical power maintains constant value, the solution to Eq.11 is:

$$h(t) = -\frac{\beta}{\alpha} + \left(h_0 + \frac{\beta}{\alpha}\right) e^{\alpha t} \tag{12}$$

where h_0 is the initial thickness at t_0, α and β are the corresponding values of the coefficients which are constant along the relevant time interval. Employing the solution given by Eq.12 for each one of the intervals introduced by the partitioning above, yields:

$$\begin{aligned} &h_1 = a_0 + b_0 h_0;\ a_0 = \frac{\beta_0}{\alpha_0}(e^{\alpha_0 T_0} - 1);\ b_0 = e^{\alpha_0 T_0} \\ &h_2 = a_1 + b_1 h_1 = a_1 + b_1 a_0 + b_1 b_0 h_0 \\ &\dots \\ &h_n = a_{n-1} + b_{n-1} a_{n-2} + b_{n-1} b_{n-2} b_{n-1} a_{n-3} + \cdots + b_{n-1} \dots b_1 a_0 + b_{n-1} \dots b_0 h_0 \end{aligned} \tag{13}$$

where only the last term, highlighted by the curly bracket, depends on the initial thickness value h_0. Here, the constants a_k, b_k are defined by:

$$a_k = \frac{\beta_k}{\alpha_k}(e^{\alpha_k T_k} - 1);\ b_k = e^{\alpha_k T_k}; k = 0, 1, \dots, n-1 \tag{14}$$

where α_k, β_k are the values of α_P, β_P, respectively, along the time interval T_K. Importantly, the last term h_0 is multiplied by a series of *n* numbers; each number b_k is smaller than unity because $\alpha(p) < 0$. Consequently, for sufficiently large number of steps *n* the last term will become arbitrary close to zero and therefore negligible compared to a_{n-1} and other terms, which indicate fading memory effect as shown in Fig.15(a) where the evolving thin liquid film 'forgets' the initial conditions as derived in Eq.13,

ii) Digital task, XOR

Fig. 13(a) describing an MZI circuit with two directional couplers and an optofluidic cell in one of the arms, which supports the nonlinear self-induced phase change effect described above, and the circuit described by Fig. 13(c) with a liquid cell placed in the coupling region, which affects the transmittance via self-induced coupling change (nonlocal effect). In both cases, the self-induced phase/coupling change due to liquid deformation invoked by the active WG is

translated into intensity changes in the output arms D_1 and D_2. To allow sufficiently large actuation of the liquid, the corresponding actuation time scale τ_l must be smaller than pulse width τ_w, whereas to ensure memory, i.e., that the liquid deformation imprinted by the $(n-1)th$ bit will affect the phase/coupling change of the nth bit, the distance between subsequent pulses τ_r must be smaller than τ_l. These ensure that the optically imprinted light pulse in the gas–liquid interface at time moment n − 1 affects the liquid through the subsequent pulse at time moment n. Since, for an optical signal of given power and operation time, thinner film is expected to introduce more significant nonlinear response (unless it is so thin that the optical signal leads to saturation due to very fast liquid depletion above the gold patch), we choose liquid thickness in the region between 0 and 0.5 μm. Below, we employ the nonlinear self-induced phase change and the self-induced coupling change (nonlinear effect) between adjacent WGs and the accompanying memory effect to perform both digital and analog tasks.

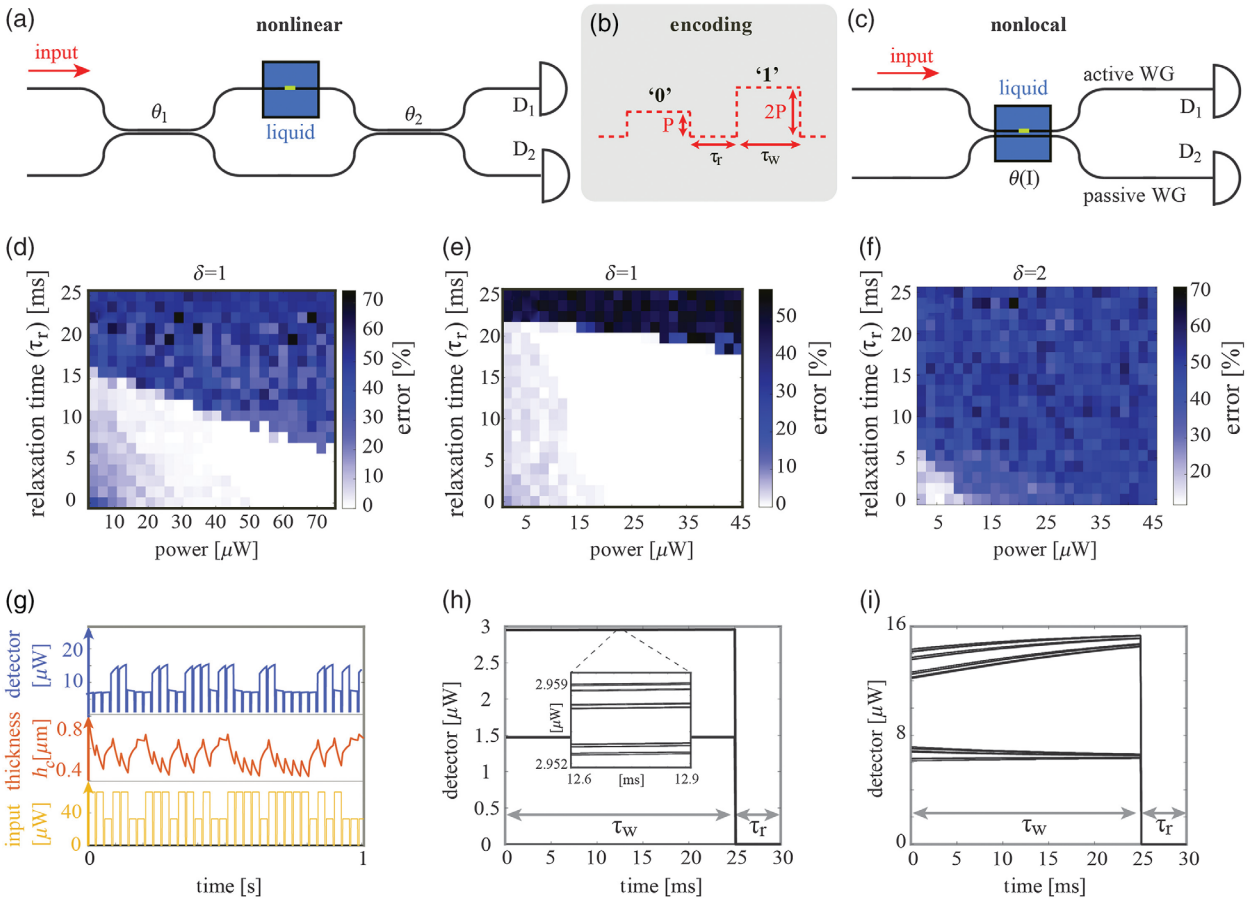

Figure 13: Simulation results presenting RC computing of the XOR task by employing self-induced phase change (nonlinear) and self-induced coupling change (nonlocal) effects. (a) Schematic diagram presenting the MZI circuit with two linear couplers, where the liquid cell introduces self-induced phase change in one of the arms measured by a pair of detectors $D_{1,2}$, (b) encoding scheme of "0" ("1"), which employs a square wave modulation with actuation period τ_w of power 2P (P), followed by relaxation period τ_r, and (c) nonlocal circuit, which employs self-induced coupling change and identical encoding. (d) Test results presenting performance error of the XOR task for delay parameter $\delta = 1$ as a function of P_{max} and relaxation time τ_r in nonlinear circuit (a), and colormap (e) performing an identical task with nonlocal circuit (c) demonstrating the enhanced area of vanishing error. (f) Test results of the XOR task with $\delta = 2$ using nonlocal circuit (c) showing minimal error ~11%. (g) Dynamics evolution of the optical signal in detector D_1 (blue) and liquid thickness h_c (red) due to the actuation signal (green) with $\tau_w = 25$ ms, $\tau_r = 5$ ms, and $P = 0.033$ mW. (h) Folded dynamics of optical intensity in the nonlinear circuit and (i) nonlocal circuit showing enhanced separability of the different regimes.

Consider the delayed XOR operation, where an arbitrary input time series $\{x_n\}_{n=1}^{N}$ $(n = 1,2,\dots,N)$ of zeros and ones is mapped to output sequence $\{y_n\}_{n=1+\delta}^{N}$ according to:

$$\{x_n\}_{n=1}^{N} \rightarrow \{y_n\}_{n=1+\delta}^{N}; \qquad y_n = x_{n-\delta} \oplus x_n \tag{11}$$

where $\oplus$ is the addition modulo, (i.e., XOR operation), and $\delta > 0$ is an integer encoding the delay. In particular, $\delta = 1$ corresponds to the simplest case of smallest delay, where the XOR operation is performed on adjacent bits, whereas $\delta = 2$ corresponds to the case where it is performed on bits that are separated by one bit. The corresponding dynamics of the thin liquid film, applicable irrespective of the nonlocal or nonlinear circuit in Fig. 11, admits the following evolution equation explicitly:

$$h_c(n) = f[h_c(n-1), P(n)] \tag{12}$$

where the state of the liquid at discrete time moment n is determined by the result of the nonlinear saturation function f, which depends on an incident power $P(n)$ at the same time n and liquid thickness at preceding time $n - 1$. This dependence describes the memory effect of the liquid film, where the finite (typically millisecond) relaxation time imprinted in the gas–liquid interface at time $n - 1$ interacts with a subsequent pulse at time n.

To implement XOR operation, we can either employ the (nonlinear) self-induced phase change or the (nonlinear– nonlocal) self-induced coupling change with circuits Figs. 13(a) and 13(c), respectively. The input series $\{x_n\}_{n=1}^{N}$ is encoded as a sequence of square pulses of power level P or $2P$ depending on the value of logic "0" or "1," as described by Fig. 13(b); the corresponding power level operates during a time τ_w and is followed by relaxation time τ_r. Figures 13(d) and 13(e) present the $P - \tau_r$ performance diagram with different colors encoding the corresponding prediction error, for the case of nonlinear circuit and nonlocal circuit described by Figs. 13(a) and 13(c), respectively. Note that the performance diagram of the nonlocal circuit presents the (white) region of vanishing error, which has a larger area compared with the corresponding area in the performance diagram of the nonlinear circuit. Furthermore, the lowest power value of the white region in the nonlinear case is ∼40 μW with a lower value around ∼10

μW for the nonlocal case. Higher performance of the nonlocal circuit stems from higher sensitivity of the intensity of the transmitted signal with respect to changes of the liquid thickness, compared with the nonlocal case. Specifically, sensitivity estimates can be determined by taking the derivative of the MZI signal due to a phase shift φ, given by $dcos^2\left(\frac{\varphi}{2}\right)/dh_c = \frac{1}{2}\sin(\varphi)\frac{d\varphi}{dh_c}$, where the derivative $\frac{d\varphi}{dh_c}$ can be estimated from Fig. 12(c), similarly, Fig.14 provides an estimate for the typical slope/sensitivity in the nonlocal case.

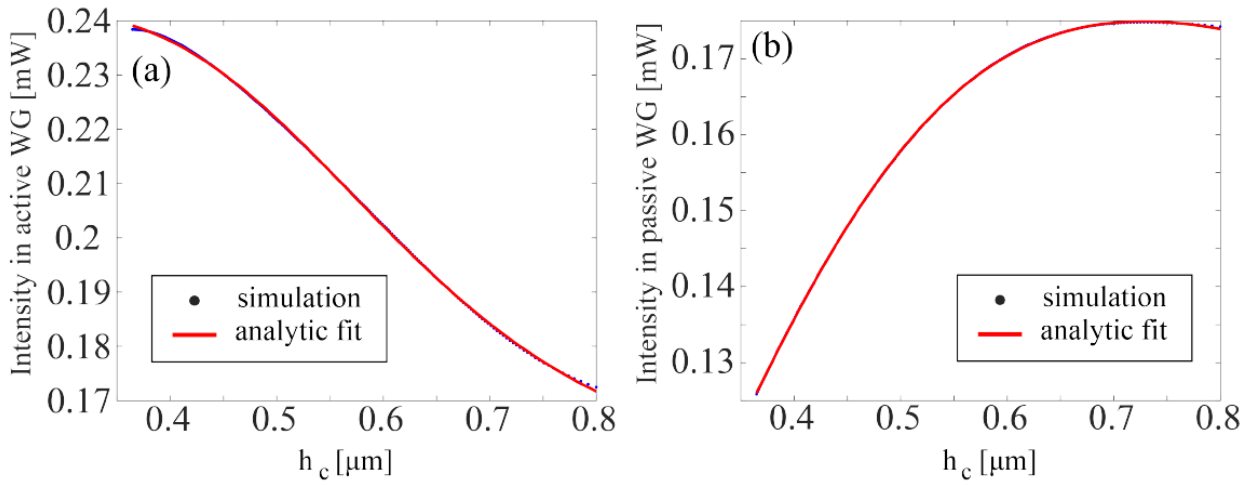

Figure 14: Multiphysics simulation result describing dependence of optical output power in active (a) as well as (b) passive WGs in a directional coupler geometry as a function of liquid film thickness, where the two parallel WGs have separation distance 500 nm (see Fig.13(c)).

To implement RC by employing our system, we first obtain a training matrix, without tuning the internal system properties, and then use this matrix to perform the test stage, which performs relevant computations. In particular, to accomplish the training stage, we first collected the output data in $D_{1,2}$ and arranged it in an $N \cdot p_w \times 2$-dimensional matrix, where N is the number of bits used for training, and p_w is the excitation time (which affects the number of rows in the output matrix). In our XOR simulation for training steps, we used $p_w = 25$, N = 1000. We then rearrange the output matrix in matrix $X = (M, N)$, where $M = 2p_w$ and each column in the

matrix X represents data from time step $i(i = 1, \dots, N)$, and use it to solve the following linear equation for the weight matrix W_{out}:

$$Y = X \cdot W_{out} \tag{13}$$

where Y is a predetermined desired output. Here, W_{out} is an $M \times 1$ dimensional vector that is determined by employing Tikhonov (ridge) regression, which is expected to be executed digitally in future experimental realizations, via MATLAB's built-in "ridge" function, which minimizes the following expression:

$$|Y - Y_T|^2 + \beta |W_{out}|^2 \tag{14}$$

where β serves as a regularization parameter, and $|\cdots|$ denotes the Euclidean norm. Note that the first term in Eq.14 penalizes large differences between the output vector Y and the desired output Y_T, whereas the second term penalizes large weight values, which facilitates better performance [49]. The corresponding closed form for W_{out} is then given as:

$$W_{out} = (X^T X + \beta I_N)^{-1} X^T Y \tag{15}$$

where non-zero β multiplies a unity matrix I_N of dimension N, thus adding nonzero values to the diagonal of matrix $X^T X$ and potentially regularizing it. To implement the test stage, we feed the previously unseen driving sequence, generate new design matrix X_{test}, and operate on it with the previously derived W_{out} via:

$$Y_{test} = X_{test} W_{out} \tag{16}$$

To finalize the computation result, the output vector Ytest is subjected to the threshold step with values above (below) 0.5 being rounded to one (zero). The corresponding error rate (E_r) is then determined by comparing the computation result after the threshold with the true result:

$$E_r = \frac{100 \times \gamma}{N_{test}} \tag{17}$$

where N_{test} is the total number of bits in the test sequence, and γ is the number of errors in the computation. For test stage of the XOR task, we employed the values $N_{test} = 20$ and $M = 50$, whereas, for "zero/one" handwritten digit classification, we employed $N = 12665$, $N_{test} = 2115$, and $M = 28 \times 28 \times 2$ weights. The corresponding ridge parameter value we used to train all models in our work was 0.01.

The enhanced performance of the nonlocal circuit for the delayed $\delta = 1$ XOR task manifests also for the $\delta = 2$ XOR task, as can be seen by comparing the corresponding $P - \tau_r$ performance diagrams of the nonlocal circuit with minimal error of ~11%, presented in Fig. 13(f), to the performance diagram of the nonlinear circuit presented in Fig.15(c) with minimal error of ~25%. In general, as can be seen from the graph in Fig.15(d), presenting the test error for a fixed P and τ_r, performance of the XOR gate quickly degrades for higher values of the delay δ, which also demonstrates prominent memory of only one time backward in time. Figure 13(g) presents the underlying dynamics of the thin liquid film (red curve) and the output signal (blue curve) in the D_1 detector in the nonlocal circuit [Fig. 13(c)], under an exciting signal (green curve).

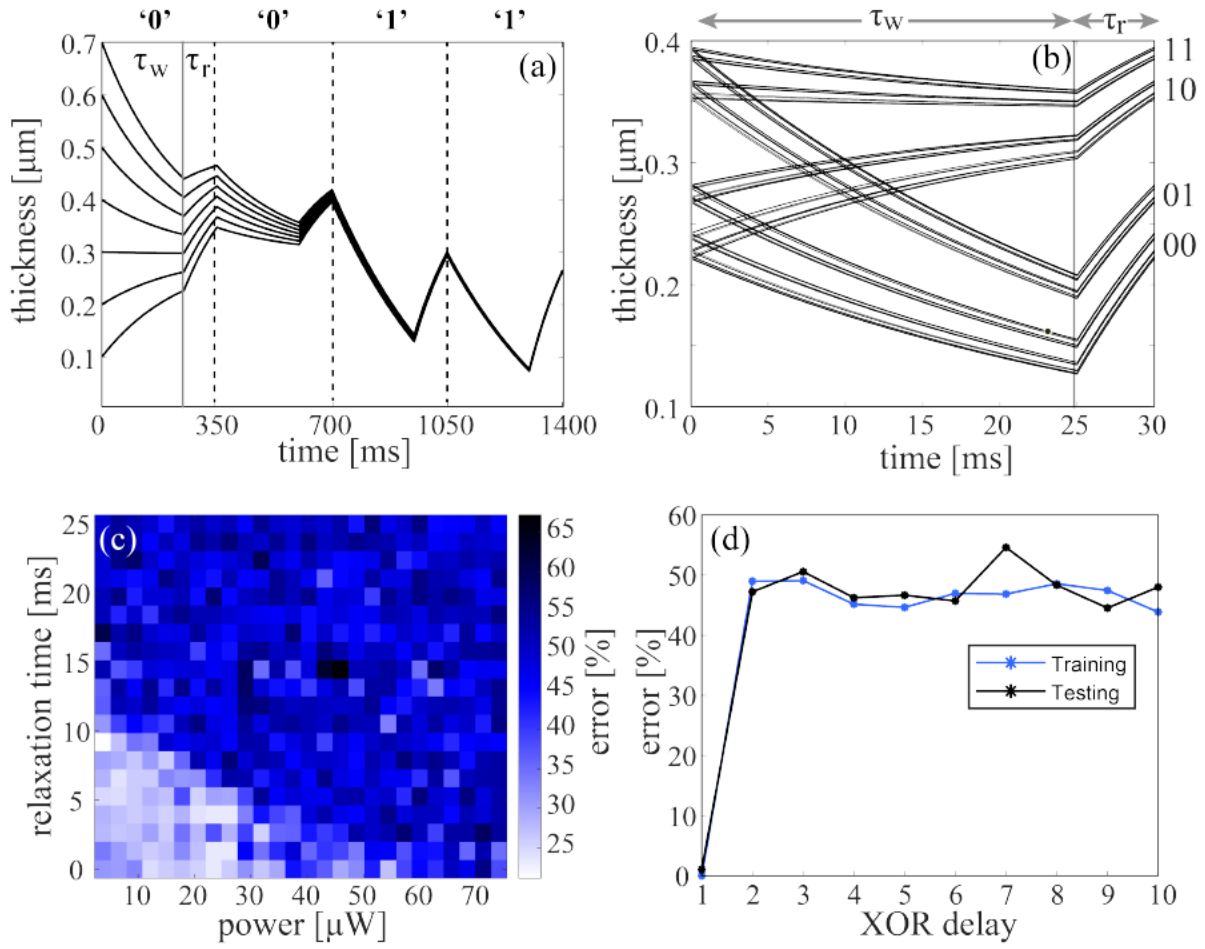

Figure 15: Numerical results presenting: (a) illustration of the fading memory effect, where the evolving system 'forgets' the different initial conditions leading to convergence towards a common attractor state; (b) folded thickness dynamics diagram where thickness evolution in nonlocal circuit is divided to time intervals of length $T = \tau_w + \tau_r$ and plotted on top for each other between times $5T$ to $200T$. The diagram shows four main curves demonstrating four different combinations due to two possible actuation pulses and one step back in time dominant memory (key parameters: τ_w = 25 ms, τ_r = 5 ms, P = 0.033 mW); (c) test results of XOR gate with delay d = 2 (τ_w= 25 ms, τ_r = 10 ms). (d) Error performance of XOR operation as a function of delay d for the following parameters: τ_w= 10 ms, τ_r= 25 ms, P = 0.06 mW.

To visually analyze the different patterns of detected power, we construct folded dynamics diagrams, where the optical signals at different time intervals of length $T = \tau_w + \tau_r$ are plotted on top of each other. Fig.13(h) and Fig.13(i) present folded dynamics graphs for the nonlinear and nonlocal circuits between times $5T$ to $200T$, respectively, where the signal in the nonlocal circuit shows enhanced separability compared to the nonlinear case performed under

similar conditions τ_w= 25 ms, τ_r = 5 ms, and P = 33 μW. Notice that Fig.13(h) and Fig.13(i) do not show dependence on initial conditions, which is in concert with the graph in Fig.15(a), demonstrating fading memory effect that the system practically "forgets" the initial conditions after 5T. More specifically, Fig. 13(i) presents four main curves with an internal substructure, corresponding to "1" or "0," which was preceded by "1" or by "0", these represent the four dominant combinations, which allow an efficient solution of the delayed (δ = 1) XOR task, whereas the internal structure represents next order memory effects, which allows us to some extent to solve the δ = 2 XOR task. More formally, since the dynamics of our system converges to states that do not depend on the initial conditions, it satisfies the so-called common-signal-induced synchronization [50], also known as echo state,8 which is a necessary property enabling a dynamical system to serve as an RC.

To determine the required optical energy E needed for training, we assume that the number of "0" and "1" pulses is equal, leading to $E = (NP/2 + NP)\tau_w$; for instance, N = 1000, P = 10 μW, and $\tau_w = 20$ ms yields E = 0.1 J. Similarly, the energy during the test stage E_{test}, required for a solution of a string of length N_{test}, is given by $E_{test} = (N_{test}P/2 + N_{test}P)\tau_w$. The case with $N_{test} = 20$ and similar parameters used during the training stage discussed above yields $E_{test} = 6$ μJ.

iii) Analog task, Hand written digit recognition

Next, we consider the classification task of hand-written "zero and "one" digits; Fig. 6(a) presents a sample of 20 images from Modified National Institute of Standards and Technology (MNIST) database [51], each of the size 28 × 28 pixels. To encode each image as a signal, without filtering or other preprocessing procedures, we partitioned the image into a set of horizontal rows or columns, where each pixel is represented by a 1-ms long constant optical

power proportional to the brightness value of the corresponding pixel. Specifically, the pixels are encoded according to power values cP_{max}, where P_{max} is the power needed to encode the brightest pixel of unity brightness ($c = 1$), whereas $c = 0$ corresponds to dark pixels that carry no features, and other values $0 < c < 1$ correspond to pixels of intermediate brightness. Figure 16(b) presents an example of a hand-written "one" digit used for classification, where the 28 ms long signal encoding the highlighted red horizontal row is given by Fig. 16(c) with left/right pixels corresponding to early/late times. To perform image classification, we employ either the nonlinear or nonlocal circuits presented in Figs. 13(a) and 13(c), respectively, where the top and bottom arms receive in parallel the 1-ms long bits encoding the ith and the following $(i + 1)$th rows, respectively, thus generating more correlations between different lines and leading to higher accuracy compared to feeding just one arm at a time. Figure 16(d) presents the classification error during the training and testing stages, with training values naturally admitting lower values. Interestingly, both errors admit fairly low values below 0.5% across a wide range of power values P_{max} spanning from 0.01 to 0.1 mW. The total energy needed to feed one image is determined by 28 × 28× 1 ms × P_{max} × c, where c is the average brightness level of the image laying between $0 < c < 1$ and typically admitting value ~0.15. The corresponding energy for the training/testing stage is achieved by multiplying the one image energy above by the total number of corresponding images; for $P_{max} = 10$ μW, the corresponding average power level is given by $cP_{max} = 1.5$ μW.

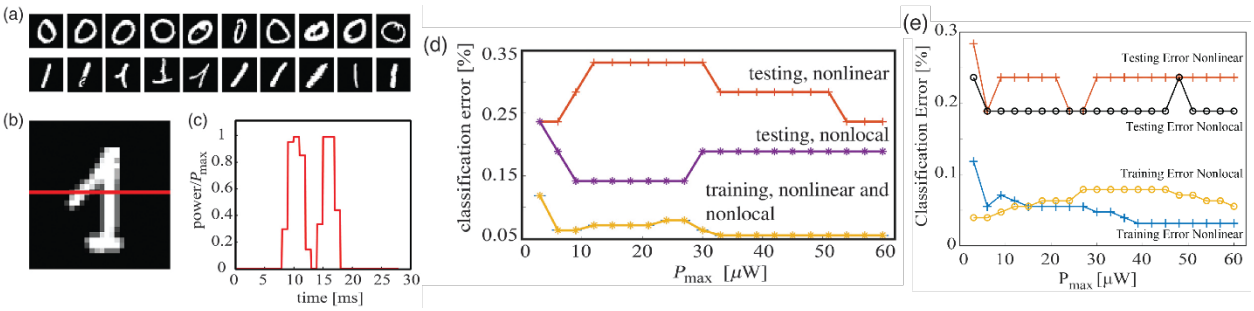

Figure 16: RC of analog task: classification of hand-written "zero" and "one" digits. (a) Sample of 20 images each of size 28 × 28 pixels, which were used for classification. (b) Detailed "one" image with (c) presenting the encoded signal along a single red horizontal row; the bits of two adjacent rows are injected in parallel into the two input arms of nonlocal [Fig. 13(a)] or nonlinear [Fig. 13(c)] circuits. (d) Classification error of both training and test stages, each employing 12665 and 2115 images, respectively. The nonlocal circuit with minimal error of 0.14% demonstrates enhanced performance compared to the nonlinear circuit with minimal error of 0.24%. Employing just one arm of the MZI for bits injection, i.e., injecting only one row at a time, increases the classification error for nonlinear circuits to ~0.55% for similar P_{max} values. (e) Handwritten 'zero'/'one' classification based on parallel columns injection into nonlinear and nonlocal circuits.

To learn more about the role of the reservoir in our modality, we also performed linear regression analysis, where the output signal is made equal to the input signal, which is followed by ridge regression, allowing us to obtain the corresponding weights that perform the corresponding task with corresponding error given by 0.61%. Interestingly, employing a reservoir presented in Fig. 13(a) but without liquid response yields similar 0.61% error for "zero/one" digit classification, which is around 4.3 times higher compared to the best 0.14% reservoir performance for this task. It is worth mentioning that the performance described in Fig. 13(d) and Fig.16(e) is not a prominent function of the optical power and using larger power does not lead to significantly enhanced performance. While in this work the input data used for the analog task were not subject to any preprocessing, we expect that common methods such as edge detection should improve the accuracy.

iv) Network scalability

Fig.17 presents numerical simulation result of RC of NARMA2 task (which will be introduced in chapter 2) as a function of number of liquid cells and the number of inputs/outputs (reservoir size) in the photonic network. The number of time steps used for training is 400 whereas for testing is 100 throughout the considered cases with maximal power 0.1 mW. Fig.17(a) presents RC results with an MZI hosting a single liquid cell in one of the arms, demonstrating very good agreement between the predicted and the actual signals with average normalized mean square error (NMSE) value 0.0023. Fig.17(b) presents a schematic description of photonic WGs network where each intersection is a symmetric directional coupler, and each rectangle is a liquid cell. In such architecture the number of layers is equal to the number of inputs/outputs (reservoir size), and facilitates signal mixing from all input WGs prior to arrival to the output layer. Fig.17(c) presents NMSE as a function of reservoir size due to RC performed in circuits described in Fig.17(b) (for which the reservoir size is 8). In particular, reservoir size 0 indicates linear regression-based performance without utilizing the reservoir, hence indicating that employing reservoir size 2 already improves the performance by a factor of ~ 2.5, whereas naively increasing the reservoir size does not lead to significant improvement for the specified values. The latter suggests that further optimization could be made, and in fact Fig.S17(d) presents NMSE values as a function of number of liquid cells in a reservoir presented Fig.17(b), where the liquid cells are positioned randomly across the photonic circuit. Interestingly, increasing the number of cells beyond 8 does not significantly improve the performance. It is worth mentioning that in the studied optofluidic system the most dominant short-term memory is one step back in time, and hence computation accuracy reduces as a function NARMA order. For completeness, NMSE values of testing stage for NARMA2, NARMA3 and NARMA 4 tasks are

0.0023, 0.0485 and 0.0596, respectively, whereas the corresponding NMSE values obtained by implementing linear regression only are given by 0.0054, 0.063 and 0.0595.

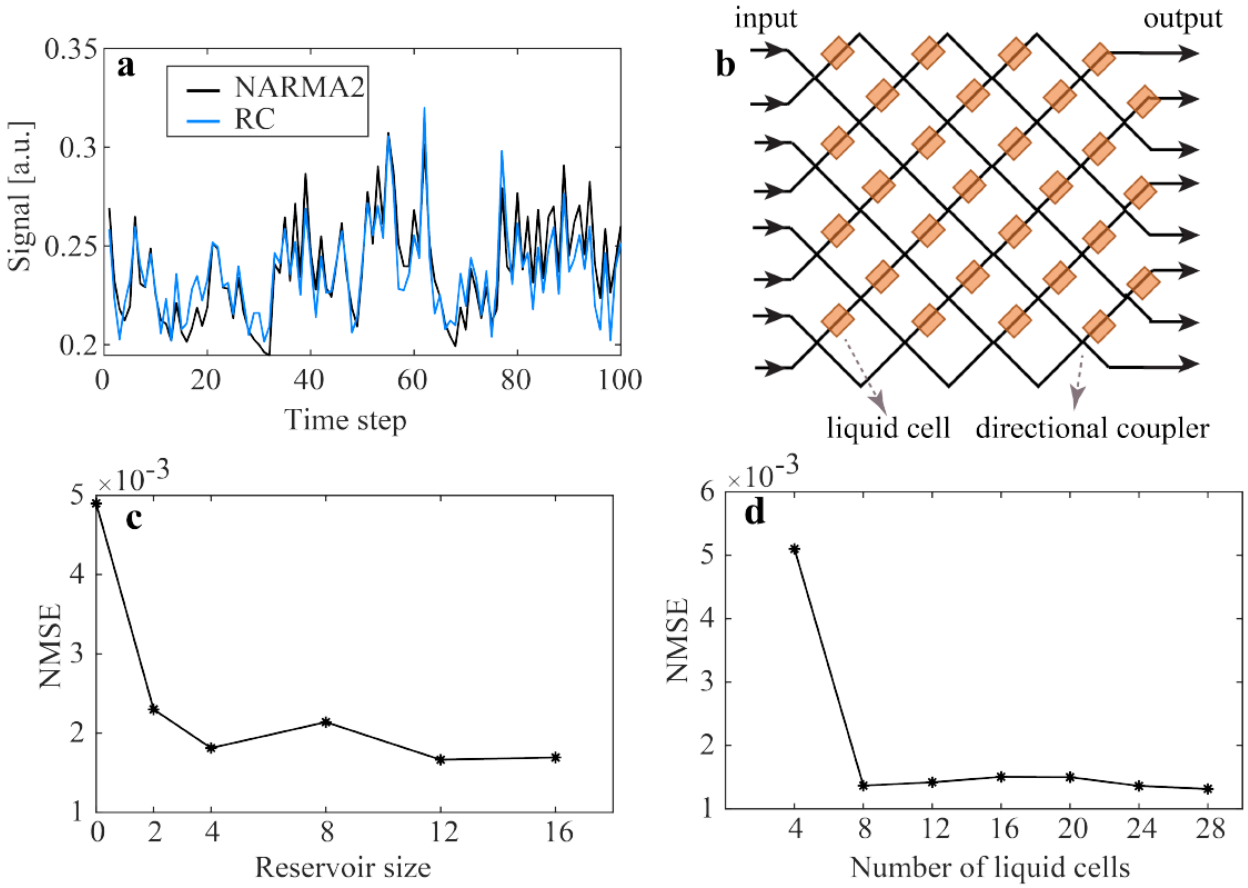

Figure 17: Numerical results demonstrating RC of NARMA2 task using optofluidic circuits as a function of number of inputs/outputs as well as number of liquid cells. (a) Comparison between RC result and the actual values demonstrating low NMSE value 0.0023. (b) Typical architecture of photonic circuits used to study NARMA2 performance as a function of reservoir size and number of liquid cells. (c) NMSE as a function of reservoir size (number of input/output WGs), demonstrating improvement compared to the case without reservoir (labeled as '0'). In all cases only single liquid cell is used. (d) NMSE as a function of number of liquid cells in a network with a fixed number of eight inputs/outputs, and placing liquid cells in random position.

b) Experiment

i) Digital task

Similar to what we have done in simulation, we start from XOR task, encode logical '0' and '1' as low and high-power levels P_0 and P_1, respectively, where each of the pulses admits

duration time τ_w and is followed by a pulse of weaker non-zero power level P_r and duration τ_r. The latter enables relaxation of thin liquid film towards initial non-deformed state and also to monitor fringes movement also during τ_r time intervals, which would not be possible if P_r would vanish. Fig.18(a) presents induced phase change values (blue curve) due to a random input sequence of 0's and 1's (red curve) with: τ_w= 50 ms, τ_r= 10 ms, P_0 = 8 mW, P_1 = 20 mW, and P_r = 1 mW. While the time response in Fig.18(a) presents strong correlation between the magnitude of latest optical pulse to the value of the self-induced phase change, e.g., higher power latest optical pulse leads also to higher value of optical phase change, in practice, it can be noted even with a naked eye, that there are some patterns which are indicative of the memory carried by previous pulses in the sequence which affect the latest pulse. In order to highlight the memory effect and the correlation between the latest pulse and the pulse preceding it, we plot all time intervals of length $\tau_w + \tau_r$ = 60 ms on top of each other in Fig.18(b) which describe emergence of four clusters similar to Fig.15(b). Here, the clusters are labeled as '11', '10', '01', '00' where the left and right indices stand for the preceding and the latest optical pulses of power P_0 or P_1, respectively. In particular, the latest pulse '1' leads to peak which belongs to either '11' (red) or to '01' (blue) cluster, whereas preceding pulse '0' leads to either '10' (green) or to '00' (black) cluster. Note that formation of four clusters indicate that the different peaks are grouped irrespective of their location in the time-series, thus realizing echo-state property.

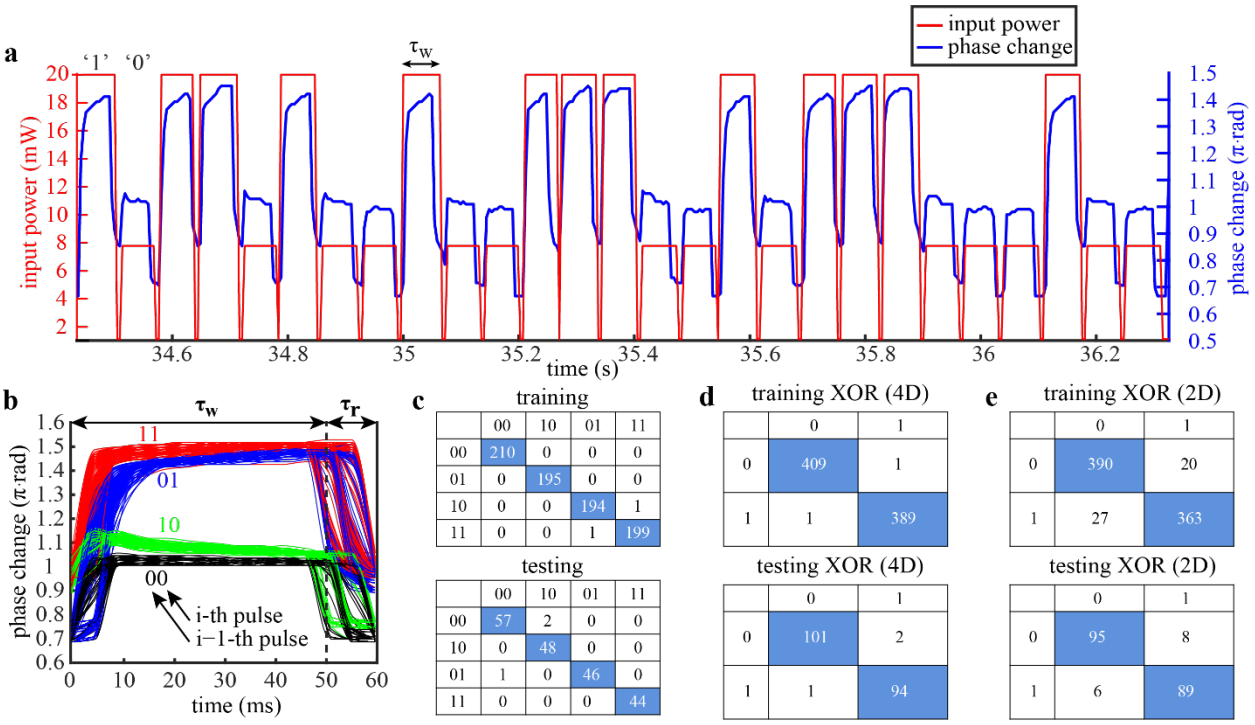

Figure 18: Experimental demonstration of RC which relies on the self-induced phase change effect. (a) Phase change response due to TC-driven deformation of 0.5 μm thick silicone oil film under a sequence of square wave pulses of duration τ_w = 50 ms and relaxation time τ_r = 10 ms, with power levels $P_{0,1}$ encoding logical '0' and '1'. Here, the optical power levels P_0 and P_1 lead to phase change values of approximately π rad and 1.4π rad, respectively. (b) Folded dynamics plot where all pulses of time τ_w and relaxation τ_r are plotted on top of each other along the interval of duration $\tau_w + \tau_r$ revealing four dominant clusters classified according the previous (i-1-th) and latest (i-th) pulse. (c) Confusion matrices of the 00, 01, 10, 11 classifications where the vertical axis corresponds to actual (input) values whereas horizontal axis corresponds to predicted (output) values. (d,e) Confusion matrix of XOR task based on preliminary 4D and 2D classification, respectively.

In order to accomplish RC task, we inject a random sequence of 1000 pulses with power levels $P_{0,1}$, and acquire the dynamics of the optical phase by using the CCD camera at the output of photonic YI. We then use the first 800 pulses to accomplish the training stage, digitally achieved by solving the linear ridge regression equation and obtaining the teaching matrix. At the next testing stage, we feed 1000−800−2 = 198 bits, where a factor of two describes elimination of one bit at the beginning (because XOR requires two input bits) and for

convenience one bit in the end. We then acquire the corresponding dynamics as a function of time, and digitally apply the teaching matrix on the measured signal to perform the computation.

Fig.18(c) presents the confusion matrices for the training and the testing stages of the classification of '00', '01', '10', '11' temporal sequences (considered as mapping {00, 01, 10, 11} → {00, 01, 10, 11} and referred below as 4D case), whereas Fig.18(d) presents the corresponding performance of XOR task if '00' and '11' are associated with '0', whereas '01' and '10' are associated with '1' (considered as mapping {00, 01, 10, 11} → {0, 1} and referred below as 2D case). Fig.18(e), on the other hand, presents direct XOR task computation without employing the 4D space, showing less prominent performance presumably due to less effective usage of the underlying memory.

ii) Liquid-based optical memory analyses

Unsurprisingly, increasing τ_r leads to more pronounced loss of memory of the preceding pulse due to more complete relaxation of the gas-liquid interface, hence resulting in test error increase presented in Fig.19(a). To quantify the notion of memory we represent each one of the self-induced phase change curves in Fig.18(b) along the interval $\tau_w + \tau_r$, as a point in the principal components (PCs) space. Specifically, by keeping the two dominant PCs in the corresponding PC expansion of each one of the curves, we expect to obtain four different clusters corresponding to each one of the groups. We then enclose each cluster by corresponding standard deviation ellipsoid, indicative of variance (σ) of points' distribution along each one of the axes, and define the degree of separation between the different groups by considering intersection of the corresponding ellipses where small/large intersection indicates high/large separation due to strong/weak memory. With this in mind, assuming that the total area occupied by all ellipses is ST we define the following non-dimensional memory parameter M:

$$M = \frac{S_T - S_I}{S_T} \tag{18}$$

where SI is the intersection area of different ellipses. Fig.19(b-d) represents the curves as points in PC1-PC2 plane where PC1 and PC2 are the first two PCs, and the axes of the corresponding standard deviation ellipses along each direction are equal to 2σ.

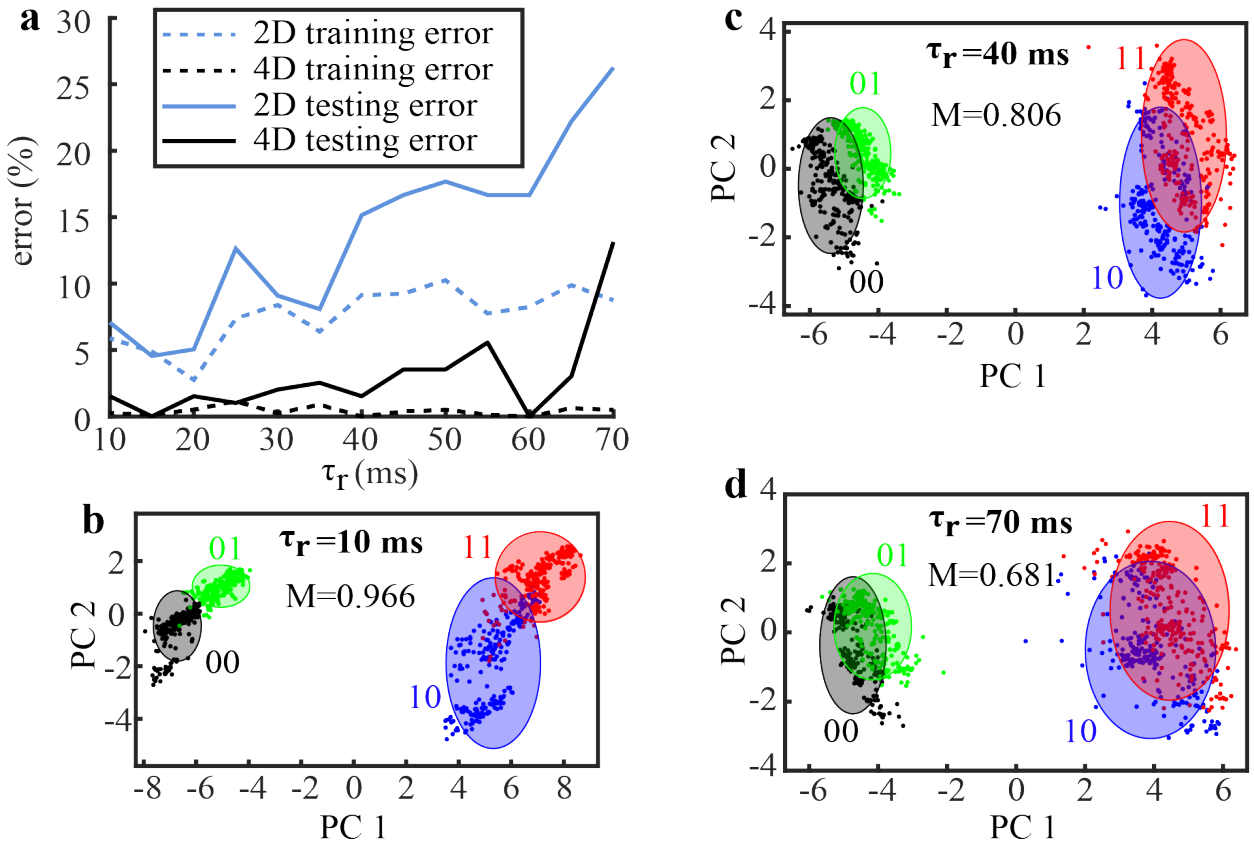

Figure 19: Experimental demonstration of RC performance and memory as a function of relaxation time. (a), Testing error as a function of time difference between successive pulses, τ_r, varying between 10 ms to 70 ms at steps of 5 ms. (b-d) PCA diagrams of first two PCs (PC1-PC2 plane) for increasingly higher values of τ_r: (b) - 10 ms, (c) - 40 ms, (d) - 70 ms, indicating increasingly lower separation of the standard deviation ellipses and corresponding lower values of the memory parameter M = 0.966, 0.806, 0.681.

Since $S_I < S_T$ holds, the parameter M is subject to $0 \leq M \leq 1$, where the limit cases M = 0 and M = 1 are realized when $S_I = 0$ and $S_I = S_T$, respectively. Notably, the ellipses in Fig.19(b-

d) admit increasingly higher intersection (lower separation between '11' and '10', and '01' and '00' states) for increasingly higher relaxation times τ_r = 10, 40, 70 ms with corresponding values M = 0.966, 0.806, 0.681, respectively. While in our RC approach we employed relatively slow CCD camera, given the fact that TC-driven actuation of liquid films can support oscillations on kHz scale, it is possible to achieve faster computation if one employs line detectors which offer faster acquisition time.

iii) Analog task

Fig.20 presents experimental results of handwritten 0 − 9 digits recognition (MNIST data set as we used in simulation) using the MZI structure as we used in Fig.10(a). In our experiments we down sampled the image from 28 × 28 to 14 × 14 to ensure that fiber-chip coupling does not change during the computation time, and also implement row-by-row injection of the image where the power level of the optical pulse is proportional to the brightness of the corresponding pixel, and duration of each optical pulse is 4 ms without any relaxation time in between. Fig.20(b) presents a typical encoded signal injected to the reservoir, implementing row by row image injection, as well as response signal after it passed through the reservoir. The corresponding confusion matrix summarizing RC classification of handwritten 0 − 9 digits is given in Fig.20(c), indicating better performance for more distinct digits (e.g., 0 and 1) and high error values (encoded as % in the colorbar) for less distinct digits (e.g., 4 and 9).

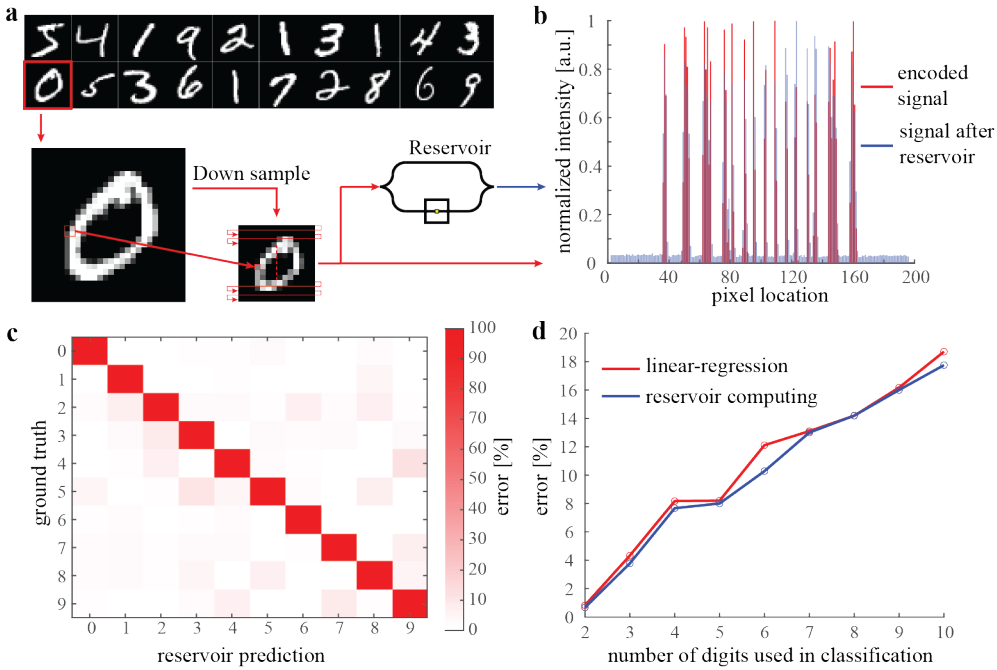

Figure 20: Experimental results demonstrating RC of MNIST task using optofluidic MZI. (a) Sample of the 28 × 28 digits images that were down-sampled to 14 × 14 images and subsequently injected into the optofluidic MZI circuit with one of the arms. (b) Typical encoded input signal and the resultant output signal after the reservoir of a single raw in one of the digits. (c) Confusion matrix for 0-9 digits classification with colormap encoding the corresponding error. (d) Performance as a function of number of digits, demonstrating lower error by using reservoir compared to linear regression.

Fig.20(d) presents classification performance of 0−1, 0−2, ... 0−9 sets where the red line stands for linear regression (LR) result, which does not rely on physical reservoir, whereas the second row presents optofluidic RC result showing lower error for all tasks (except task 0 − 7 of similar performance) and most significant relative error reduction for 0 − 1 and 0 − 2 cases, given by 100 × (0.83 − 0.67)/0.83 = 19.2% and 12.7%. Interestingly, when doing experiments, we noticed that RC efficiency of the classification task takes place at actuation pulse power P_{max} = 13 mW, which corresponds to a slightly ruptured liquid surface and relatively high values of self-induced phase change. However, higher P_{max} values, which in turn lead to more prominent ruptured state and higher nonlinearity, do not provide better classification accuracy. It may suggest that in this case the dynamics becomes chaotic, which is not conducive to achieve

efficient RC, and may furthermore imply that error values of RC computation may be also used to classify the degree of chaos present in the system.

7. Summary and discussion

In this work, we employ chip-scale silicon photonic platform with a partially exposed WG, facilitating controlled light-heat-liquid interaction where the photonic mode affects the geometry of the gas-liquid interface via TC-driven liquid transport, whereas evolving shape of the liquid film surface translates into changes of the photonic mode phase. Notably, the observed optical effect takes maximal phase change values between $1.4 - 1.8\ \pi\cdot$ rad in the steady state regime, and approximately $0.65\ \pi\cdot$ rad in the oscillatory regime, depending on initial liquid thickness, which is more than one order of magnitude higher compared to the more traditional TO effect in solid materials. Even higher phase change values are expected if higher optical power is used or more efficient optical dissipation takes place. Furthermore, our results reveal non-trivial dependence of the nonlinear phase change as a function of liquid thickness, which was achieved by employing drop-by-drop electrostatic deposition of femtoliter silicone oil droplets under fixed periodic actuation which can reach several kHz. Our 3D simulation results provide good quantitative agreement against the experimental results in the pre-rupture regime, and can further stimulate the development of computational methods to capture ruptured dynamics of the liquid film, hysteresis effects due to pinning effects and non-uniform substrate properties, and instability of the optically thin liquid films which leads to sharp changes in the self-induced phase values above threshold values. We then employ the self-induced phase change effect to demonstrate that liquid film is capable to serve as an optical memory capable to support beyond von-Neumann computational architecture where memory is a part of the computation.

Remarkably, the active area of the nonlinear response due to liquid deformation takes place in a region of few micrometers and does not require additional feedback lines which are needed in electronic systems or in hybrid photonic-electronic systems. In particular, we experimentally demonstrate the capability to perform with high accuracy digital XOR task as well as enhance the performance of MNIST digits classification analog task compared to a linear-based classifier. Finally, we employ NARMA2 task to test RC performance of more elaborate photonic integrated circuits with varying liquid cell configurations and reservoir sizes. Our results indicate that even a small number of liquid cells can significantly improve computation accuracy, indicating a non-trivial relationship between circuit structure and computation.

Our methodology and results provide a clear path to pursue versatile fundamental research directions aiming to explore intriguing optical properties such as long-range nonlocal interaction between adjacent WGs due to liquid deformation, resonant-based absorption due to excitation of localized surface plasmon polaritons (as opposed to non-resonant metal patch employed above), and also spatial and temporal properties of nematic-isotropic phase change effects of liquid crystals due to local temperature increase. Providing further detailed understanding of the various factors that affect the self-induced phase change effect may lead to an extension of our work where longer memory effects enable computation applications with higher bit data. Furthermore, the connection of our optofluidic system to NC may stimulate exploration of intricate light-liquid interaction processes with computation applications, including emulation of biological neuron activity which also takes place in liquid environment.

Acknowledgement

Chapter 1, in part, is a reprint of the material as it appears in Advanced Photonics 4, no. 4 (2022) and Nature Communications 14, no. 1 (2023). The original publications have been re-arranged for clarity for the reader. The dissertation author is the first author of this paper, with co-authors Prabhav Gaur, Shimon Rubin, and Yeshaiahu Fainman.

Chapter 2 - Polarization Division Multiplexing (PDM) for photonic physical reservoir computing

1. Background

The unique training method of RC require mapping the input to a high dimensional space, the dimensionality of this high dimensional space directly influences the performance of the RC system, with higher dimensions generally leading to better performance. The dimensions can be related to the number of independent reservoir outputs, corresponding to the number of channels in the system. So, to enhance the performance of a PRC system, directly scaling up the number of parallel photonic devices in the network is the most straight forward way, but it will be footprint-expensive, since a typical photonic MZI modulator is hundreds of micrometers size, while a typical electrical transistor is tens of nanometers nowadays [52]. Another option is increasing the reservoir dimensions by applying division multiplexing technologies to increase the channel densities in the system, such as wavelength division multiplexing (WDM). While WDM require wavelength sensitive devices such as MRM, may not create fully independent channels in other devices such as MZI. Apart from WDM, polarization division multiplexing (PDM) has been widely used for optical communication-based applications[53][54], which could also be used in photonic-based PRC systems.

A typical photonic waveguide is designed to be thin and wide to get a large difference between its Transverse Electric (TE) and Transverse Magnetic (TM) effective mode indices, minimizing the potential cross-talk between the modes to reduce loss. Due to this difference in effective mode indices, the TE and TM modes will exhibit distinct responses to the same material modulation. When both modes are presented in the waveguide, their varying responses lead to elliptical polarization inside the waveguide. Elliptically polarized light carries information about the electric field components E_x and E_y, as well as the phase difference σ

between them, which leads to the definition of Stokes Parameters [55]. Therefore, at least 3 independent output channels could be obtained from PDM in a photonic reservoir.

In this chapter, we utilize a recently demonstrated Hybrid-Photonic-Electronic (HPE) system as the PRC platform[56], which use electro-optic phase shifter in a MZI to encode data and apply feedback. After the photonic chip, we use a free-space optical system to demultiplex the polarization information, serving as the network's output for reservoir computing. By benchmarking the system with the NARMA10 task, we demonstrate through numerical simulations and experiments that PDM enhances the performance of photonic-based PRC by increasing its channel density.

2. Hybrid-Photonic-Electronic Reservoir Computing system

The framework of a typical HPE-RC system is shown in Fig. 21(a), the reservoir layer consists of K parallel blocks, where each node can be realized by various photonic structures, such as MZI arrays in previous demonstration [56]. In this study, we utilize a simple MZI structure with thermal phase shifters on both arms as our block to demonstrate the effect of PDM on photonic-based physical RC in a clear and concise way.

Fig.21(b) presents the details of the k-th block, the input data vector u(n) is encoded into a voltage signal applied to the first heater of the MZI with a scaling factor φ_k. The optical output of the MZI will pass through the free-space PDM setup which will be described in next session. The PDM output will be converted into an electrical signal vector $x_k(n)$, then the feedback voltage based on previous outputs with bias θ_k and scaling factor α_k is applied to the MZI's second heater as $\theta_k + \alpha_k f(x_k(n-1), \dots, x_k(n-\tau))$. Here f is the feedback function of previous τ outputs, which could be their average, for instance. After the reservoir layer, ridge

regression is applied as the linear classifier to compute the weights vector w, as described in previous chapter, enabling the calculation of output vector $y(n) = x(n) \cdot w$.

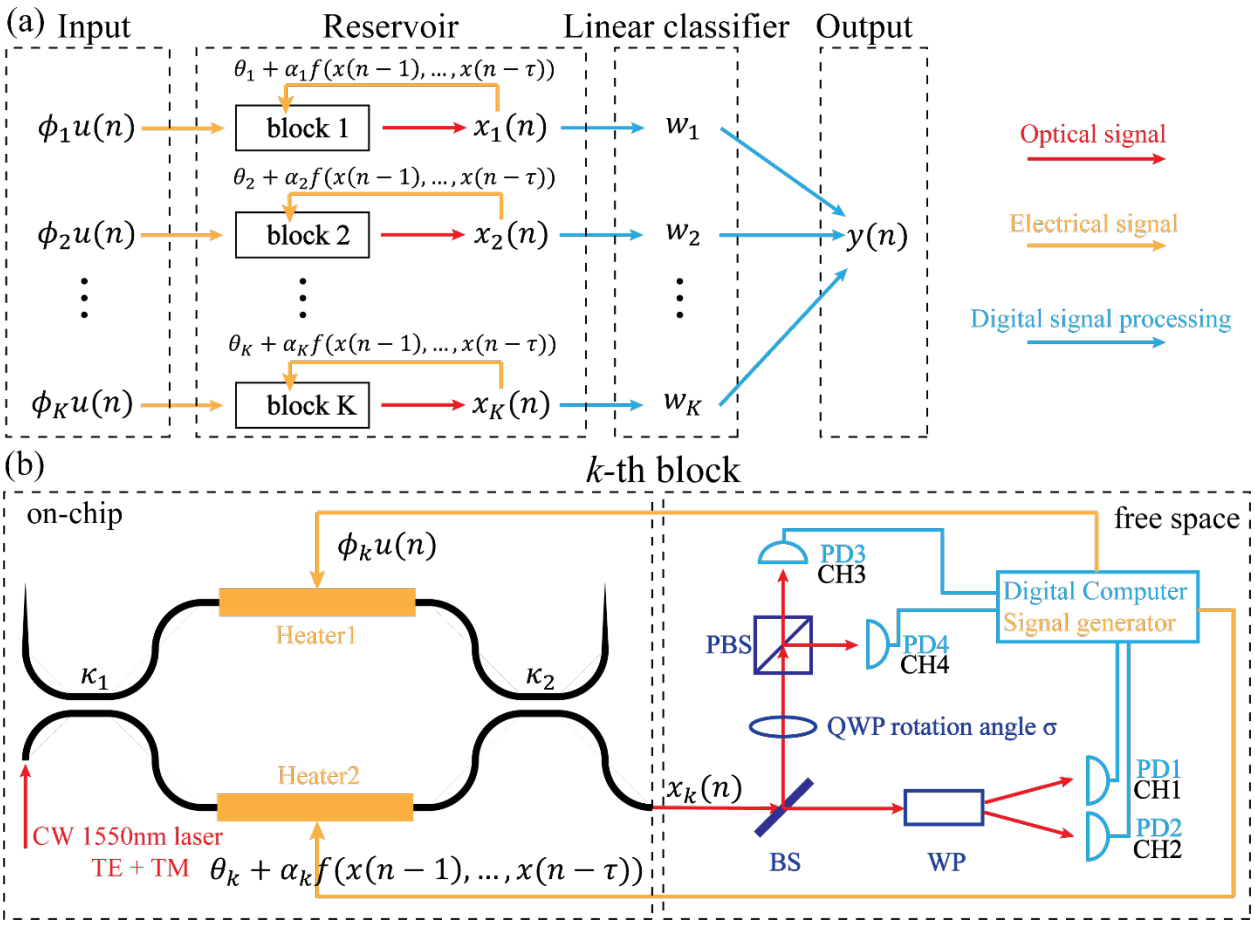

Figure 21: (a) Schematic diagram of the HPE-RC system. The reservoir layer comprises K parallel blocks, each leveraging photonic structures for data I/O and processing. After the reservoir is a linear classifier for system output. (b) Detailed illustration of a single block that is used in this paper, which consists of a MZI structure on the photonic chip and PDM setup in the free space. On the photonic chip, 45° linearly polarized 1550 nm CW laser excite both TE and TM mode in the waveguide is used as information carrier. Input vector u(n) is encoded into a voltage signal applied to the first heater of the MZI. The feedback signal calculated from previous outputs is applied to the second heater. In free space, PDM is achieved by splitting the MZI output into 4 channels by passing through combinations of QWP and PBS. BS: beam splitter, PBS: polarization beam splitting, WP: Wollaston Prism, QWP: quarter waveplate

The cross-sectional view of the waveguide and heater is shown in Fig.22(a). We use silicon waveguide with 500 nm width and 220 nm thickness, positioned between 2 μm thermal silicon dioxide substrate and 2.2 μm PECVD silicon dioxide cladding layer. The thermal phase

shifter is a 400×4×0.2 μm TiW alloy patch, placed on top of the cladding layer, the resistance of the heater is measured to be 384 Ω. A 300 nm PECVD SiO_2 passivation layer is sitting on top to protect the heater.

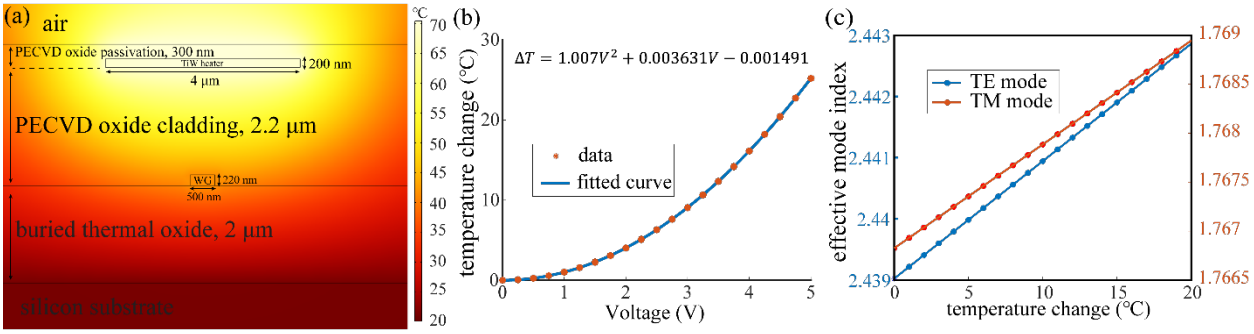

Figure 22: (a) Cross-sectional view of the silicon waveguide and thermal phase shifter used in the HPE-RC system. Also presenting the simulated steady state temperature distribution in the colormap when 5V is applied on the heater. (b) Simulation and fitting result of the applied voltage on the heater versus induced temperature change in the waveguide. (c) simulation result of the relationship between the temperature change in the waveguide and the effective mode indices for TE and TM modes.

The transfer function of the MZI is given by:

$$\begin{pmatrix} E_{out1} \\ E_{out2} \end{pmatrix} = \begin{pmatrix} \sqrt{1-\kappa_2} & i\sqrt{\kappa_2} \\ i\sqrt{\kappa_2} & \sqrt{1-\kappa_2} \end{pmatrix} \begin{pmatrix} e^{-i\psi_1} & 0 \\ 0 & e^{-i\psi_2} \end{pmatrix} \begin{pmatrix} \sqrt{1-\kappa_1} & i\sqrt{\kappa_1} \\ i\sqrt{\kappa_1} & \sqrt{1-\kappa_1} \end{pmatrix} \begin{pmatrix} E_{in1} \\ E_{in2} \end{pmatrix} \quad (17)$$

Where E represents the input/output of two ports, κ is the power splitting ratio of the couplers, and $\phi = (2\pi/\lambda)nL$ is the phase delay of the two delay lines, where λ is the optical wavelength, n, L is the effective mode refractive index and the length of the delay lines, respectively. We use $L = 400$ μm in this study.

When the voltage V is applied to the heater, the current will induce a change in temperature to the waveguide. We use COMSOL Multiphysics® software to simulate this process, Fig.22(a) presents the steady-state temperature distribution when $V = 5$ V. The change in temperature will change the refractive index of silicon linearly by the thermo-optic coefficient $dn/dT = 1.8 \times 10^{-4}(1/Kelvin)$ [36], which will change the effective mode index. Fig.22(b)

shows the steady state average temperature change in the waveguide versus the applied voltage, which can be fitted by:

$$\Delta T = 1.007V^2 + 0.003631V - 0.001491 \tag{18}$$

Fig.22(c) presents the simulated effective TE and TM mode index versus temperature change in the waveguide, which can be linearly fitted by:

$$\begin{aligned} n_{TE} &= 1.919 \times 10^{-4}\Delta T + 2.439 \\ n_{TM} &= 9.042 \times 10^{-5}\Delta T + 1.767 \end{aligned} \tag{19}$$

With these equations, we can directly relate V to the effective mode index for TE and TM mode.

3. Experimental setup and numerical simulation for PDM

We use Division-Of-Amplitude Photopolarimeter (DOAP) method for PDM [57][58], which is one of the most widely used and straightforward way to measure Stokes parameters in real time. The general principle of the DOAP method is to split the incoming beam into 4 rays by the combination of beam splitter (BS), polarizing beam splitters (PBS) and quarter waveplates (QWP), then back calculate the Stokes parameters from the measured optical intensity and the inverse of the Mueller matrices of the optical components. Mueller matrix is the transfer matrix of the Stocks parameters when light travels through an optical component [59]. DOAP method will require the fine calibration of the optical components' Mueller matrices, which is challenging, while our goal is to acquire more independent channels, no accurate Stokes parameter measurement is necessary. So, we directly use the optical intensities measured by the photodetectors (PD) I_1 to I_4 from the DOAP setup as the reservoir output.

Our DOAP setup is shown in the left part of Fig.21(b). The incoming light is split into two identical beams by a BS, one beam is directly split again by a Wollaston Prism (WP) which can be treated as a PBS, then measured by PD_1 and PD_2. The other beam will first pass through a

QWP with rotation angle σ, split by a PBS, then measure by PD_3 and PD_4, result in 4 channels in one block.

The Stokes parameters is defined as:

$$\begin{aligned} S_0 &= E_x^2 + E_y^2 \\ S_1 &= E_x^2 - E_y^2 \\ S_2 &= 2E_xE_y\,cos\,\delta \\ S_3 &= 2E_xE_y\,sin\,\delta \end{aligned} \tag{20}$$

The ideal Mueller matrices of the BS, QWP and PBS mentioned above are:

$$\begin{aligned} M_{BS} &= \frac{1}{2}\begin{pmatrix} 1 & 0 & 0 & 0 \\ 0 & 1 & 0 & 0 \\ 0 & 0 & 1 & 0 \\ 0 & 0 & 0 & 1 \end{pmatrix} \quad M_{QWP} = \begin{pmatrix} 1 & 0 & 0 & 0 \\ 0 & 1 & 0 & 0 \\ 0 & 0 & 0 & -1 \\ 0 & 0 & -1 & 0 \end{pmatrix} \\ M_{PBS_x} &= \frac{1}{2}\begin{pmatrix} 1 & 1 & 0 & 0 \\ 1 & 1 & 0 & 0 \\ 0 & 0 & 0 & 0 \\ 0 & 0 & 0 & 0 \end{pmatrix} \quad M_{PBS_y} = \frac{1}{2}\begin{pmatrix} 1 & -1 & 0 & 0 \\ -1 & 1 & 0 & 0 \\ 0 & 0 & 0 & 0 \\ 0 & 0 & 0 & 0 \end{pmatrix} \end{aligned} \tag{21}$$

The Mueller matrix of an optical component with Mueller matrix M rotated by σ degree around the principle optical axis is:

$$M(\sigma) = R(-\sigma)MR(\sigma), \text{where } R(\sigma) = \begin{pmatrix} 1 & 0 & 0 & 0 \\ 0 & \cos(2\sigma) & \sin(2\sigma) & 0 \\ 0 & -\sin(2\sigma) & \cos(2\sigma) & 0 \\ 0 & 0 & 0 & 1 \end{pmatrix} \tag{22}$$

The intensity of light with Stokes vector $S_{in} = (S_0\ S_1\ S_2\ S_3)^T$ can be calculated by $I = qS_{in}$, where $q = (1\ 0\ 0\ 0)$, so the measured intensity of PD_1 to PD_4 can be expressed as:

$$\begin{aligned} I_1 &= qM_{PBS_x}M_{BS}S_{in} \\ I_2 &= qM_{PBS_y}M_{BS}S_{in} \\ I_3 &= qM_{PBS_x}R(-\sigma)M_{QWP}R(\sigma)M_{BS}S_{in} \\ I_4 &= qM_{PBS_y}R(-\sigma)M_{QWP}R(\sigma)M_{BS}S_{in} \end{aligned} \tag{23}$$

By equations (17) to (23), we can fully simulate the reservoir outputs by the input voltage numerically. After calibrating the detailed parameters such as the resistance, length of the MZI arms and the κ of the couplers, we can fit the measured data with the simulated data. We use

Polarization Maintained (PM) fiber rotated 45° to edge couple 1550 nm CW laser into the photonic chip to get TE and TM mode with roughly same intensity in the waveguide. DIGILENT ANALOG DISCOVERY® Mixed Signal Oscilloscope (MSO) is used to read electrical signals from PD, communicate with PC and send voltage signal to the heater.

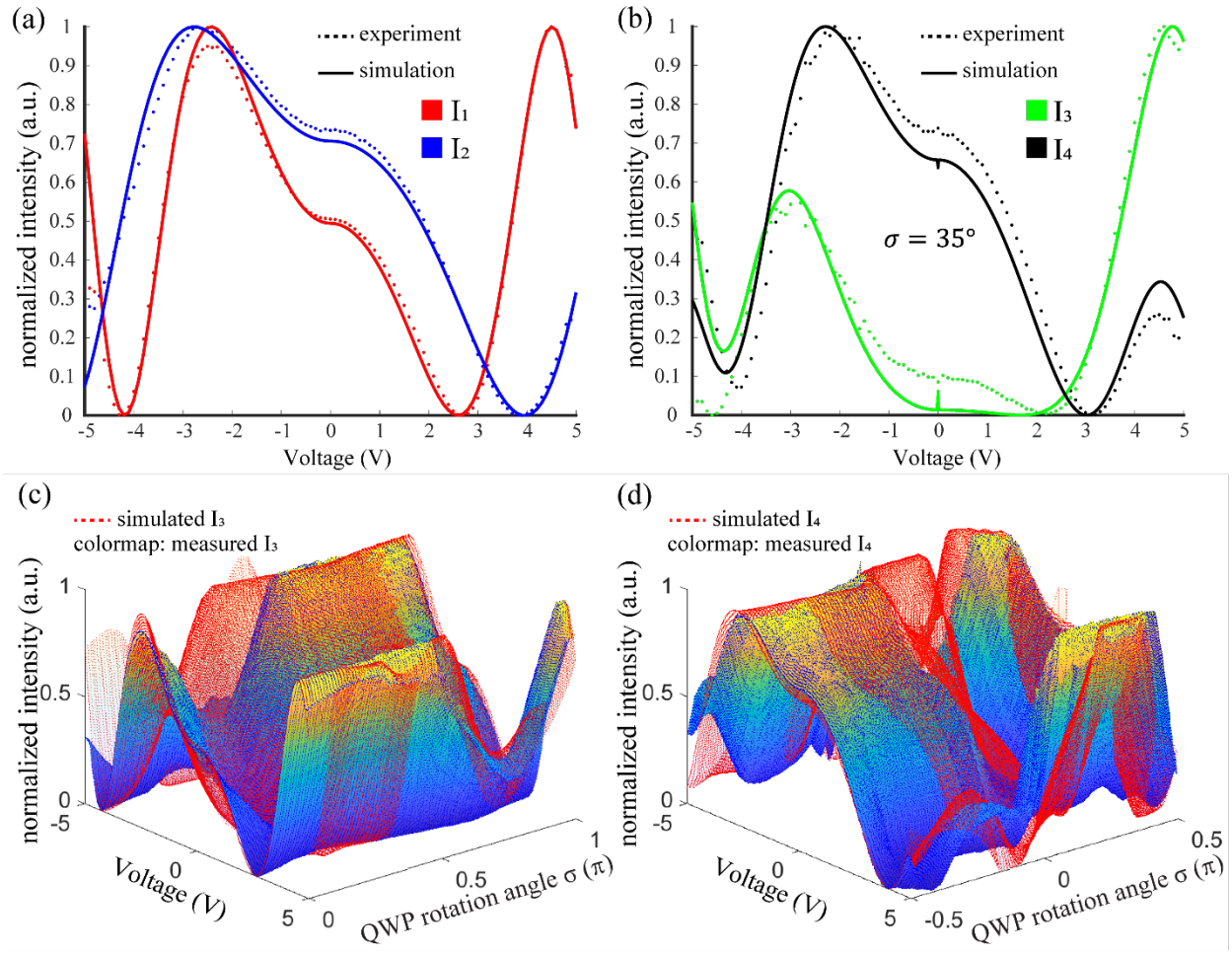

Figure 23: (a, b) Comparison of simulated (solid line) and measured (dashed line) normalized optical intensities versus applied voltage on single heater for four different PDM output channels, under $\sigma = 35°$. (c, d) Simulated (red mesh) and measured (color map) normalized optical intensities from channel 3 and 4 as a function of voltage V and QWP rotation angle σ.

Fig.23(a, b) present the normalized optical intensity versus applied voltage on the first heater when $\sigma = 35°$, comparing the simulated data (solid lines) with the measured data (dashed lines) of 4 different channels. Fig.23(c, d) present the simulated (red mesh) and the measured (colormap) I_3 and I_4 versus V and σ. We can see that the fitting of I_1 and I_2 is good, while the

fitting of I_3 and I_4 is not good enough, since TE and TM phase difference δ is very sensitive to all the optical components and we did not make perfect calibrations on them. But in general, the simulated system behavior can roughly manifest the performance of the HEP-RC system, which will be helpful for us to perform pre-experiment optimization and analyses of the reservoir system.

4. Reservoir computing performance enhancement by PDM

We perform 10th order Nonlinear AutoRegressive Moving Average (NARMA10) task as the benchmark to evaluate the performance of the PRC system. NARMA10 is a task to predict $y(n)$ by known $u(n)$, where $u(n)$ is a uniformly distributed random variable in [0,0.5], $y(n)$ is defined by:

$$y(n+1) = 0.3y(n) + 0.05y(n)\left[\sum_{i=0}^{9} y(n-i)\right] + 1.5u(n-9)u(n) + 0.1 \qquad (24)$$

We define K blocks as different random combinations of $\phi \in [0,10]$, $\theta \in [0,3]$, $\alpha \in [0,10]$ in the same MZI structure. The ranges are set to limit the input voltage to 5 Volt, which is the maximum voltage limit of the MSO. The measured voltage signal from PD will be normalized as in Fig.23. The feedback function is simply defined as the average output of the previous $\tau = 10$ steps, since we are doing 10th order NARMA. The length of the input vector u is set to $N = 1000$, the first 600 steps are used for training, and the remaining 400 steps are used for testing. The normalized mean square error (NMSE) between the predicted $\hat{y}$ and the original y is calculated as the error to evaluate the RC performance.

Before demonstrating RC tasks, we use Mutual Information (MI) analysis [60] in simulation to analyze the independence between channels and determine the optimized value of σ. Mutual information quantifies how much information about one random sequence can be

inferred by observing the other [61]. Suppose $x_i(n)$ and $x_j(n)$ are the normalized RC output sequences for the NARMA10 task from two different channels. We discretize the sequences by the 0.1 interval, leading to $D = 1/0.1 = 10$ intervals, this precision is sufficient to get accurate probability density function (PDF) while saving computational power. Then we can calculate their discrete PDF P_{x_i} , P_{x_j} and their joint PDF P_{x_i,x_j}. By these results, their MI can be calculated by:

$$I(x_i; x_j) = \sum_{a=1}^{D} \sum_{b=1}^{D} P_{x_i,x_j}(a,b) \log\left(\frac{P_{x_i,x_j}(a,b)}{P_{x_i}(a)P_{x_j}(b)}\right)$$

We simulate 1000 random blocks and scan the QWP rotation angle σ from 0 to π for each of them, after that the MI of the output sequence from CH_1 to CH_4 with regard to CH_1 is calculated. Fig.24(a) presents the average MI results of these 1000 blocks versus σ. We can see that the highest MI is 2.6 when CH_1 is compared with itself. The MI is reduced to 1.9 when comparing CH_1 with CH_2, these two channels represent the TE and TM mode, which should be two independent channels according to our setup. While for CH_3 and CH_4, their MI between CH_1 is large when σ is a multiple of $90°$, it will decrease to the lowest value of approximately 1 when σ is around multiples of $45°$, which is expected since we are using QWP. The MI result seems promising, showing obvious channel independence in our PDM setup, next we will characterize the RC performance of the system.

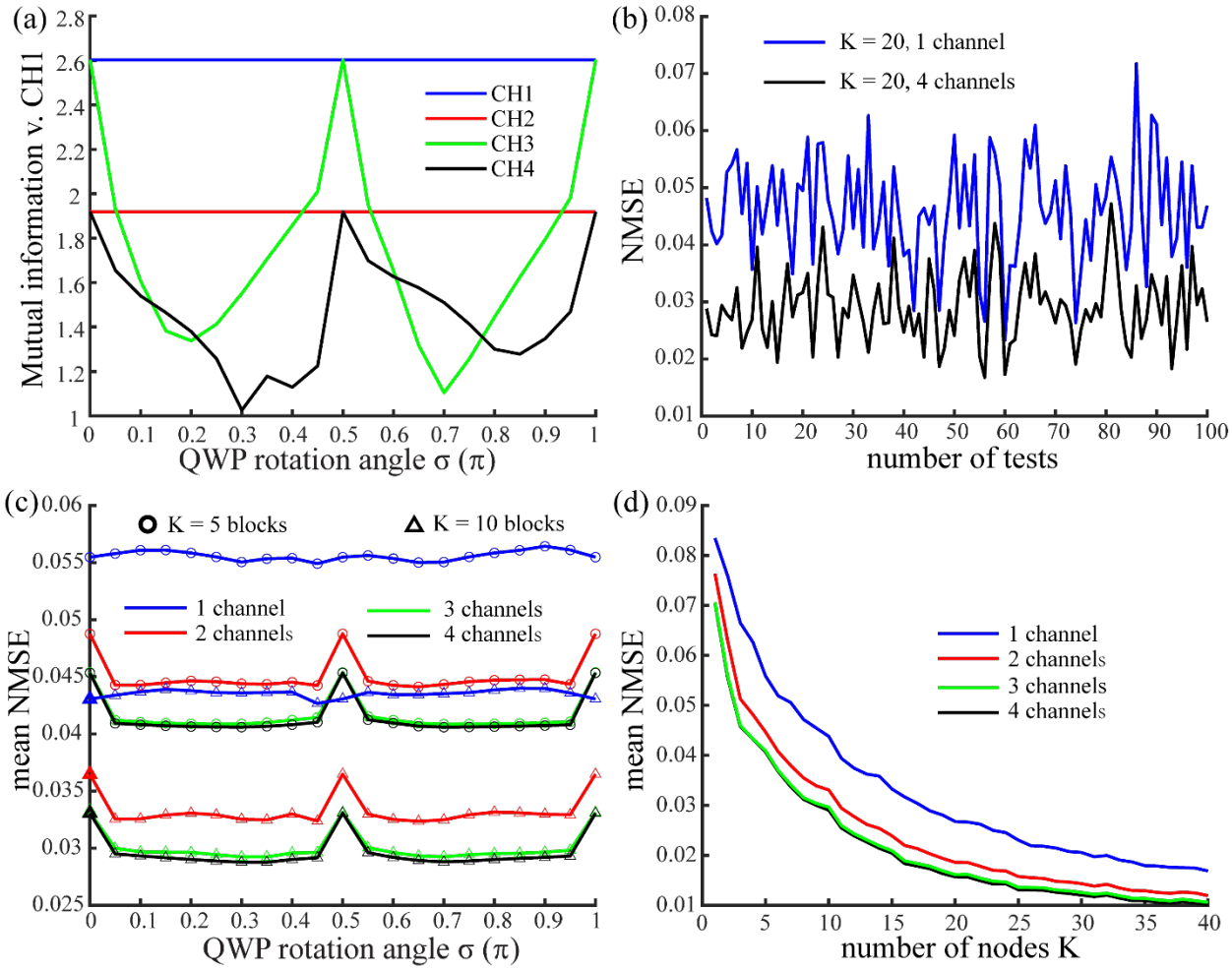

Figure 24: (a) Average mutual information between channel 1 and channel 1 to 4 versus QWP rotation angle σ. (b) Normalized mean square error (NMSE) of 100 NARMA10 tests with $K = 20$ randomly generated blocks, using the first channel (blue) and all the four channels (black), respectively. (c) Average NARMA10 test NMSE versus σ using 1 to 4 channels with $K = 5$ and 10 blocks. (d) Average NARMA10 test NMSE versus number of blocks, using 1 to 4 channels.

Randomly generated nodes lead to different RC performance. For example, Fig.24(b) presents the calculated NMSE of 100 different tests with $K = 20$ blocks and $\sigma = 45°$, using CH_1 only and all the four channels. We can see clear performance difference between these two conditions, so we can use the average NMSE of 100 random tests to evaluate the system performance more representative. Fig.24(c) shows the relation between the average NMSE and σ with different number of blocks and apply different number of channels. Notice that the mean NMSE of using a channels are calculated by taking the average NMSE of all possible C_4^a

channel combinations. We can see that the NMSE behaves similar to the MI versus σ, a smaller MI leads to better RC performance. Meanwhile, NMSE shows a significant decline when adding more blocks and channels to the system. While the effect of adding the $4th$ channel is very limited, which may correspond to the existence of only 3 independent variables when describe the polarization of light.

A more detailed number of blocks and channels versus σ relation is shown in Fig.24(d), which set $\sigma = 45°$. We can see that adding more blocks is still the best way to improve the system performance, while increase the number of channels in each block by PDM also boost up the performance. For small K value, double the number of blocks has similar effect of double the number of channels. For example, as shown in Fig.24(c), the mean NMSE value of using 10 blocks with single channel is almost the same as using 5 blocks with 2 channels, adding 3rd and 4th channel can further decrease the NMSE. The improvement of RC performance by PDM is clear now from the simulation results, next we will verify by experiment.

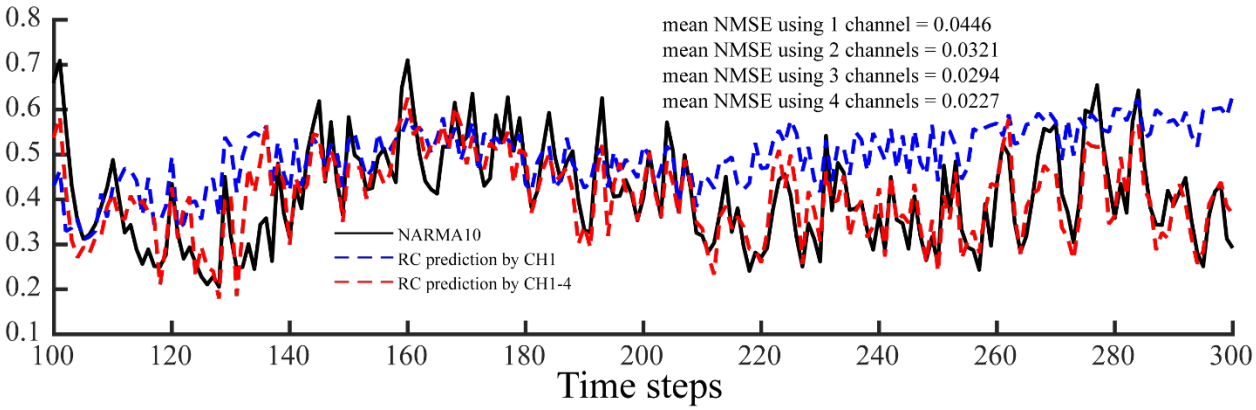

Figure 25: Comparison of original y and predicted $\hat{y}$ from experiment under $\sigma = 45°$ and $K = 10$. Black solid line is the original NARMA10 sequence, blue and red dashed line is the $\hat{y}$ calculated by using the first channel only and all four channels.

From the simulation result, we decide to use $\sigma = 45°$ in the experiment. For each time step, we apply the voltage for 0.25 ms to stabilize the temperature, record the optical signal, and turn off the heater for 0.25 ms to fully cool down the system before send in next signal. Due to

the existence of random fiber drifting in our setup, as well as some observed random glitch in the MSO, there might be random noise happened during our continuous multiple block measurement, which is hard to identify since we are doing analog measurement. To avoid the impact of random noise, we decided to run 25 randomly generated blocks and randomly pick $K = 10$ blocks for 10000 times, calculate the NMSE for each test and pick out the one with lowest NMSE. The comparison between y and $\hat{y}$ of the picked test is shown in Fig.25, we can see that when using 10 blocks with only CH_1 (blue dashed curve), the predicted $\hat{y}$ deviate a lot from the original y (black curve), the NMSE here is 0.0841. When utilize all the 4 channels, the $\hat{y}$ (dashed red curve) is much closer to y, NMSE is reduced to 0.0227. We also calculate the mean NMSE of the same test using 1 to 4 channels, which demonstrate a clear step by step decrease of NMSE from 0.0446 to 0.0227. Notice that there is still decent performance improvement between using 3 channels and 4 channels, which is different from the simulation results. We suspect that this is due to the existence of the noise that makes the channels more independent, which provide redundancy for performance improvements. This is good news for the system, since the 4th channel is again useful.

5. Conclusion and discussion

We have successful numerically and experimentally demonstrated that Polarization Division Multiplexing can be utilized to enhance the performance of photonic based Physical Reservoir Computing system by increasing the channel density in the system while keep the number of physical devices unchanged. We use the DOAP setup for PDM, which is originally proposed to measure the Stokes parameters of the light. It takes 3 independent variables to fully describe the polarization state of the light, so in theory PDM can increase 2 independent channels to the photonic PRC system, that is what we observed from the simulation result. DOAP setup

has 4 channels, the RC performance of using all 4 channels is almost the same as using 3 channels. But in experiment where all kinds of noise come into play, adding the 4th channel still boost the system performance. This indicates that the existence of noise diminishes the correlation between the PDM channels, making them more independent, which is a good demonstration of the 'black box' nature of a physical reservoir.

The blocks we studied are still randomly generated, so we have to run large enough number of tests to get statistically significant results. Notice that we used mutual information to quantify the independency between different channels from PDM, it can also be used to evaluate the independency between different blocks. We can use this method to determine the combination of nodes for best RC performance, which has been demonstrated in our previous work [56].

This paper is a preliminary demonstration of idea, so the PDM is done in free-space, which means huge footprint. However, on-chip PDM has been demonstrated by lots of groups [62][63]; the components required to duplicate our free-space setup to the chip such as polarization splitter [64] and polarization rotator [65] has also been demonstrated as well. So in the future, we can integrate both photonic blocks and PDM components on the same photonic chip to significantly decrease the system footprint. Meanwhile, increasing the channel density by PDM is more advantageous in terms of system footprint compare to directly add more blocks, since the typical size of a photonic modulator for information encoding such as MZI will be hundreds of micrometers, while on chip polarization splitter, polarization rotator and photo detector [66] are mostly in tens of micrometer size. On the other hand, the thermal-based electro-optic modulation can be replaced by other modulation technic such as PN junction [67] and $LiNbO_3$ based modulator [68], which offer much higher modulation speed and power efficiency.

In conclusion, PDM has proved to be a simple and cost-effective solution to enhance the performance of a photonic-based physical RC system, which could serve as an easy add-on technique for the future photonic RC researches.

Acknowledgement

Chapter 2, in part, is currently being prepared for submission for publication of the material with co-authors Vladimir Fedorov, Prabhav Gaur, Shimon Rubin, and Yeshaiahu Fainman.

REFERENCES

[1] Mekawey, Hosam, Mohamed Elsayed, Yehea Ismail, and Mohamed A. Swillam. "Optical interconnects finally seeing the light in silicon photonics: Past the hype." *Nanomaterials* 12, no. 3 (2022): 485.

[2] Zhou, Hailong, Jianji Dong, Junwei Cheng, Wenchan Dong, Chaoran Huang, Yichen Shen, Qiming Zhang et al. "Photonic matrix multiplication lights up photonic accelerator and beyond." *Light: Science & Applications* 11, no. 1 (2022): 30.

[3] Ribeiro, Antonio, Alfonso Ruocco, Laurent Vanacker, and Wim Bogaerts. "Demonstration of a 4× 4-port universal linear circuit." *Optica* 3, no. 12 (2016): 1348-1357.

[4] Hsueh, Tzu-Chien, Yeshaiahu Fainman, and Bill Lin. "Optical Comb-Based Monolithic Photonic-Electronic Accelerators for Self-Attention Computation." *IEEE Journal of Selected Topics in Quantum Electronics* (2024).

[5] Feldmann, Johannes, Nathan Youngblood, C. David Wright, Harish Bhaskaran, and Wolfram HP Pernice. "All-optical spiking neurosynaptic networks with self-learning capabilities." *Nature* 569, no. 7755 (2019): 208-214.

[6] Xu, Zhihao, Tiankuang Zhou, Muzhou Ma, ChenChen Deng, Qionghai Dai, and Lu Fang. "Large-scale photonic chiplet Taichi empowers 160-TOPS/W artificial general intelligence." *Science* 384, no. 6692 (2024): 202-209.

[7] Vandoorne, Kristof, Pauline Mechet, Thomas Van Vaerenbergh, Martin Fiers, Geert Morthier, David Verstraeten, Benjamin Schrauwen, Joni Dambre, and Peter Bienstman. "Experimental demonstration of reservoir computing on a silicon photonics chip." *Nature communications* 5, no. 1 (2014): 3541.

[8] Shen, Yichen, Nicholas C. Harris, Scott Skirlo, Mihika Prabhu, Tom Baehr-Jones, Michael Hochberg, Xin Sun et al. "Deep learning with coherent nanophotonic circuits." *Nature photonics* 11, no. 7 (2017): 441-446.

[9] Zhou, Tiankuang, Xing Lin, Jiamin Wu, Yitong Chen, Hao Xie, Yipeng Li, Jingtao Fan, Huaqiang Wu, Lu Fang, and Qionghai Dai. "Large-scale neuromorphic optoelectronic computing with a reconfigurable diffractive processing unit." *Nature Photonics* 15, no. 5 (2021): 367-373.

[10] Ashtiani, Farshid, Alexander J. Geers, and Firooz Aflatouni. "An on-chip photonic deep neural network for image classification." *Nature* 606, no. 7914 (2022): 501-506.

[11] Pai, Sunil, Zhanghao Sun, Tyler W. Hughes, Taewon Park, Ben Bartlett, Ian AD Williamson, Momchil Minkov et al. "Experimentally realized in situ backpropagation for deep learning in photonic neural networks." Science 380, no. 6643 (2023): 398-404.

[12] Xue, Zhiwei, Tiankuang Zhou, Zhihao Xu, Shaoliang Yu, Qionghai Dai, and Lu Fang. "Fully forward mode training for optical neural networks." *Nature* 632, no. 8024 (2024): 280-286.

[13] Fernando, Chrisantha, and Sampsa Sojakka. "Pattern recognition in a bucket." In *European conference on artificial life*, pp. 588-597. Berlin, Heidelberg: Springer Berlin Heidelberg, 2003.

[14] Milano, Gianluca, Giacomo Pedretti, Kevin Montano, Saverio Ricci, Shahin Hashemkhani, Luca Boarino, Daniele Ielmini, and Carlo Ricciardi. "In materia reservoir computing with a fully memristive architecture based on self-organizing nanowire networks." *Nature materials* 21, no. 2 (2022): 195-202.

[15] Gao, Chengkuan, Prabhav Gaur, Shimon Rubin, and Yeshaiahu Fainman. "Thin liquid film as an optical nonlinear-nonlocal medium and memory element in integrated optofluidic reservoir computer." *Advanced Photonics* 4, no. 4 (2022): 046005-046005.

[16] Gao, Chengkuan, Prabhav Gaur, Dhaifallah Almutairi, Shimon Rubin, and Yeshaiahu Fainman. "Optofluidic memory and self-induced nonlinear optical phase change for reservoir computing in silicon photonics." *Nature Communications* 14, no. 1 (2023): 4421.

[17] Tanaka, Gouhei, Toshiyuki Yamane, Jean Benoit Héroux, Ryosho Nakane, Naoki Kanazawa, Seiji Takeda, Hidetoshi Numata, Daiju Nakano, and Akira Hirose. "Recent advances in physical reservoir computing: A review." *Neural Networks* 115 (2019): 100-123.

[18] Borghi, Massimo, Claudio Castellan, Stefano Signorini, Alessandro Trenti, and Lorenzo Pavesi. "Nonlinear silicon photonics." *Journal of Optics* 19, no. 9 (2017): 093002.

[19] Corcoran, Bill, Christelle Monat, Christian Grillet, David J. Moss, Benjamin J. Eggleton, Thomas P. White, Liam O'Faolain, and Thomas F. Krauss. "Green light emission in silicon through slow-light enhanced third-harmonic generation in photonic-crystal waveguides." *Nature photonics* 3, no. 4 (2009): 206-210.

[20] Gaeta, Alexander L., Michal Lipson, and Tobias J. Kippenberg. "Photonic-chip-based frequency combs." *nature photonics* 13, no. 3 (2019): 158-169.

[21] Silverstone, Joshua W., Damien Bonneau, Kazuya Ohira, Nob Suzuki, Haruhiko Yoshida, Norio Iizuka, Mizunori Ezaki et al. "On-chip quantum interference between silicon photon-pair sources." *Nature Photonics* 8, no. 2 (2014): 104-108.

[22] Assanto, Gaetano, and Marco Peccianti. "Spatial solitons in nematic liquid crystals." *IEEE journal of quantum electronics* 39, no. 1 (2003): 13-21.

[23] Patsyk, Anatoly, Uri Sivan, Mordechai Segev, and Miguel A. Bandres. "Observation of branched flow of light." *Nature* 583, no. 7814 (2020): 60-65.

[24] Rubin, Shimon, Brandon Hong, and Yeshaiahu Fainman. "Subnanometer imaging and controlled dynamical patterning of thermocapillary driven deformation of thin liquid films." *Light: Science & Applications* 8, no. 1 (2019): 77.

[25] Fomenkov, Igor, David Brandt, Alex Ershov, Alexander Schafgans, Yezheng Tao, Georgiy Vaschenko, Slava Rokitski et al. "Light sources for high-volume manufacturing EUV lithography: technology, performance, and power scaling." *Advanced Optical Technologies* 6, no. 3-4 (2017): 173-186.

[26] Rubin, Shimon, and Yeshaiahu Fainman. "Nonlocal and nonlinear surface plasmon polaritons and optical spatial solitons induced by the thermocapillary effect." *Physical Review Letters* 120, no. 24 (2018): 243904.

[27] Rubin, Shimon, and Yeshaiahu Fainman. "Nonlinear, tunable, and active optical metasurface with liquid film." *Advanced Photonics* 1, no. 6 (2019): 066003.

[28] Marangoni, Carl. "Ueber die Ausbreitung der Tropfen einer Flüssigkeit auf der Oberfläche einer anderen." *Annalen der Physik* 219, no. 7 (1871): 337-354.

[29] Pearson, J. R. A. "On convection cells induced by surface tension." *Journal of fluid mechanics* 4, no. 5 (1958): 489-500.

[30] Levich, Veniamin Grigorevich, and Charles W. Tobias. "Physicochemical hydrodynamics." *Journal of The Electrochemical Society* 110, no. 11 (1963): 251C.

[31] Wedershoven, H. M. J. M., C. W. J. Berendsen, J. C. H. Zeegers, and A. A. Darhuber. "Infrared laser induced rupture of thin liquid films on stationary substrates." *Applied physics letters* 104, no. 5 (2014).

[32] COMSOL Multiphysics v. 6.0. www.comsol.com. COMSOLAB, Stockholm, Sweden.

[33] Mesaritakis, Charis, Vassilis Papataxiarhis, and Dimitris Syvridis. "Micro ring resonators as building blocks for an all-optical high-speed reservoir-computing bit-pattern-recognition system." *JOSA B* 30, no. 11 (2013): 3048-3055.

[34] Duree Jr, Galen C., John L. Shultz, Gregory J. Salamo, Mordechai Segev, Amnon Yariv, Bruno Crosignani, Paolo Di Porto, Edward J. Sharp, and Ratnakar R. Neurgaonkar. "Observation of self-trapping of an optical beam due to the photorefractive effect." *Physical review letters* 71, no. 4 (1993): 533.

[35] Rotschild, Carmel, Oren Cohen, Ofer Manela, Mordechai Segev, and Tal Carmon. "Solitons in Nonlinear Media with an Infinite Range of Nonlocality: First Observation<? format?> of Coherent Elliptic Solitons and of Vortex-Ring Solitons." *Physical review letters* 95, no. 21 (2005): 213904.

[36] Komma, J., Christophe Schwarz, Gerd Hofmann, Daniel Heinert, and Ronny Nawrodt. "Thermo-optic coefficient of silicon at 1550 nm and cryogenic temperatures." *Applied physics letters* 101, no. 4 (2012).

[37] McLaughlin, David W., David J. Muraki, Michael J. Shelley, and Xiao Wang. "A paraxial model for optical self-focussing in a nematic liquid crystal." *Physica D: Nonlinear Phenomena* 88, no. 1 (1995): 55-81.

[38] Conti, Claudio, Marco Peccianti, and Gaetano Assanto. "Route to nonlocality and observation of accessible solitons." *Physical review letters* 91, no. 7 (2003): 073901.

[39] Assanto, Gaetano, and Marco Peccianti. "Spatial solitons in nematic liquid crystals." *IEEE journal of quantum electronics* 39, no. 1 (2003): 13-21.

[40] Boyd, Robert. *Contemporary nonlinear optics*. Academic Press, 2012.

[41] Zhang, Yi, Shuyu Yang, Andy Eu-Jin Lim, Guo-Qiang Lo, Christophe Galland, Tom Baehr-Jones, and Michael Hochberg. "A compact and low loss Y-junction for submicron silicon waveguide." *Optics express* 21, no. 1 (2013): 1310-1316.

[42] Zhang, Yanzhen, Benliang Zhu, Yonghong Liu, and Gunther Wittstock. "Hydrodynamic dispensing and electrical manipulation of attolitre droplets." Nature communications 7, no. 1 (2016): 12424.

[43] Choi, Dongwhi, Horim Lee, Do Jin Im, In Seok Kang, Geunbae Lim, Dong Sung Kim, and Kwan Hyoung Kang. "Spontaneous electrical charging of droplets by conventional pipetting." *Scientific reports* 3, no. 1 (2013): 2037.

[44] Xie, Jingwei, Jiang Jiang, Pooya Davoodi, Madapusi P. Srinivasan, and Chi-Hwa Wang. "Electrohydrodynamic atomization: A two-decade effort to produce and process micro-/nanoparticulate materials." *Chemical engineering science* 125 (2015): 32-57.

[45] De Gennes, Pierre-Gilles. "Wetting: statics and dynamics." *Reviews of modern physics* 57, no. 3 (1985): 827.

[46] Bonn, Daniel, Jens Eggers, Joseph Indekeu, Jacques Meunier, and Etienne Rolley. "Wetting and spreading." *Reviews of modern physics* 81, no. 2 (2009): 739-805.

[47] Delmas, Mathieu, Marc Monthioux, and Thierry Ondarçuhu. "Contact angle hysteresis at the nanometer scale." *Physical review letters* 106, no. 13 (2011): 136102.

[48] Giacomello, Alberto, Lothar Schimmele, and Siegfried Dietrich. "Wetting hysteresis induced by nanodefects." *Proceedings of the National Academy of Sciences* 113, no. 3 (2016): E262-E271.

[49] Lukoševičius, Mantas. "A practical guide to applying echo state networks." In *Neural Networks: Tricks of the Trade: Second Edition*, pp. 659-686. Berlin, Heidelberg: Springer Berlin Heidelberg, 2012.

[50] Inubushi, Masanobu, Kazuyuki Yoshimura, Yoshiaki Ikeda, and Yuto Nagasawa. "On the characteristics and structures of dynamical systems suitable for reservoir computing." *Reservoir computing: theory, physical implementations, and applications* (2021): 97-116.

[51] Deng, Li. "The mnist database of handwritten digit images for machine learning research [best of the web]." *IEEE signal processing magazine* 29, no. 6 (2012): 141-142.

[52] Cao, Wei, Huiming Bu, Maud Vinet, Min Cao, Shinichi Takagi, Sungwoo Hwang, Tahir Ghani, and Kaustav Banerjee. "The future transistors." *Nature* 620, no. 7974 (2023): 501-515.

[53] Goossens, Jan-Willem, Mansoor I. Yousefi, Yves Jaouën, and Hartmut Hafermann. "Polarization-division multiplexing based on the nonlinear Fourier transform." *Optics express* 25, no. 22 (2017): 26437-26452.

[54] Ivanovich, Darko, Samuel B. Powell, Viktor Gruev, and Roger D. Chamberlain. "Polarization division multiplexing for optical data communications." In *Optical Interconnects XVIII*, vol. 10538, pp. 160-178. SPIE, 2018.

[55] Stokes, George Gabriel. "On the composition and resolution of streams of polarized light from different sources." *Transactions of the Cambridge Philosophical Society* 9 (1851): 399.

[56] Gaur, Prabhav, Chengkuan Gao, Karl Johnson, Shimon Rubin, Yeshaiahu Fainman, and Tzu-Chien Hsueh. "Information Processing in Hybrid Photonic Electrical Reservoir Computing." *arXiv preprint arXiv:2404.01479* (2024).

[57] Azzam, R. M. A. "Division-of-amplitude photopolarimeter (DOAP) for the simultaneous measurement of all four Stokes parameters of light." *Optica Acta: International Journal of Optics* 29, no. 5 (1982): 685-689.

[58] Negara, Christian. "Different designs for a polarization state detector based on division-of-amplitude." In *Proceedings of the 2016 Joint Workshop of Fraunhofer IOSB and Institute for Anthropomatics, Vision and Fusion Laboratory*, vol. 33, pp. 85-107. J. Beyerer and A. Pak (KIT Scientific, Karlsruhe, 2017), 2017.

[59] Fujiwara, Hiroyuki. *Spectroscopic ellipsometry: principles and applications*. John Wiley & Sons, 2007.

[60] Cover, Thomas M., and Joy A. Thomas. "Entropy, relative entropy and mutual information." *Elements of information theory* 2, no. 1 (1991): 12-13.

[61] Thomas, M. T. C. A. J., and A. Thomas Joy. *Elements of information theory*. Wiley-Interscience, 2006.

[62] Lin, Zhongjin, Leslie Rusch, Yuxuan Chen, and Wei Shi. "Chip-scale, full-Stokes polarimeter." *Optics express* 27, no. 4 (2019): 4867-4877.

[63] Fang, Liang, Shuang Zheng, and Jian Wang. "Design of on-chip polarimetry with Stokes-determined silicon photonic circuits." *Optics Express* 29, no. 20 (2021): 31026-31035.

[64] Kim, Dong Wook, Moon Hyeok Lee, Yudeuk Kim, and Kyong Hon Kim. "Planar-type polarization beam splitter based on a bridged silicon waveguide coupler." *Optics express* 23, no. 2 (2015): 998-1004.

[65] Aamer, Mariam, Ana M. Gutierrez, Antoine Brimont, Diedrik Vermeulen, Gunther Roelkens, Jean-Marc Fedeli, Andreas Hakansson, and Pablo Sanchis. "CMOS compatible silicon-on-insulator polarization rotator based on symmetry breaking of the waveguide cross section." *IEEE Photonics Technology Letters* 24, no. 22 (2012): 2031-2034.

[66] Jacob, Ajey P., Sujith Chandran, Joris Van Campenhout, Marianna Pantouvaki, John Heck, Ken Giewont, Michal Rakowski, Yusheng Bian, Peter Debackere, and Matthias Kuntz. "Photonic-integrated circuit fabrication and test approaches." In *Integrated Photonics for Data Communication Applications*, pp. 369-410. Elsevier, 2023.

[67] Reed, Graham T., Goran Mashanovich, F. Yand Gardes, and DJhttps Thomson. "Silicon optical modulators." *Nature photonics* 4, no. 8 (2010): 518-526.

[68] Zhu, Di, Linbo Shao, Mengjie Yu, Rebecca Cheng, Boris Desiatov, C. J. Xin, Yaowen Hu et al. "Integrated photonics on thin-film lithium niobate." *Advances in Optics and Photonics* 13, no. 2 (2021): 242-352.